INSTANTANEOUS ENERGY SEPARATION IN SHEAR LAYER

B. Han and R. J. Goldstein

Department of Mechanical Engineering
University of Minnesota
Minneapolis, MN 55455, U.S.A

ABSTRACT

A numerical study is performed to investigate energy separation in a shear layer. The unsteady two dimensional Navier-Stokes equation and total-energy equation are solved using an equal-order linear finite element and fractional four-step method. The predicted results show that the pressure fluctuations due to the vortex motion in the shear layer cause the energy separation. The results for instantaneous velocities and temperatures agree well with experimental data.

INTRODUCTION

Spontaneous separation of the total temperature in different portions of a high speed flow is called "energy separation". Energy separation presents the possibility to heat or cool fluid without using a conventional heating or cooling system. However, current obtainable temperature differences between hot and cold regions are not large enough for practical engineering systems. Further research to enlarge the temperature difference is still required. Not only this possibility, but the ability to predict and understand the accurate temperature distribution in fluid flows is critical to many engineering applications where flows are used as heat transfer enhancement methods such as impinging jets.

This phenomenon was observed in the early 1940's from measurement [1] of the recovery temperature distribution on a circular cylinder in a high speed air stream. Other researchers have reported the existence of energy separation in various flows including boundary layers [2], jet flows [3, 4], cross flow across a circular cylinder [5], and shear flows [6]. With the results of these studies, Eckert [7] suggested the physical explanation of the mechanism of energy separation. Two different mechanisms can cause energy separation in fluid flows. One is the imbalance between the energy transport by viscous shear work and that by heat conduction. The other is the pressure fluctuation within flow fields due to the transport of vortices. Energy separation in real flow fields can be due to combined mechanisms of the imbalance and the pressure fluctuations.

Even though previous research improved understanding on energy separation, it has several limitations. First is the lack of instantaneous velocity and temperature information. Only a few researchers tried to measure the instantaneous temperature in the wake of a cylinder [8], however most previous research is based on time-averaged temperature measurements. To verify previously proposed physical models and make them complete, instantaneous temperature and velocity information is essential. Second, previous numerical studies [5, 9] were performed with invisicd fluid assumption. However, a vortex is formed in flows through entrainment of surrounding fluid, in which viscosity plays vital role.

In the present study two dimensional plane shear layer is numerically simulated to investigate the instantaneous energy separation mechanism. Unsteady two dimensional Navier-Stokes equations and total energy equation are solved. The results will provide useful information to understand the instantaneous mechanism of energy separation.

MATHEMATICAL AND NUMERICAL FORMULATION

The calculation domain and coordinate system for the two-dimensional flow system are illustrated in Figure 1. Two air streams with different velocity (U_1, U_2) are initially separated by a splitter plate. After merging of the two streams, a shear layer is formed and grows as flow goes downstream.

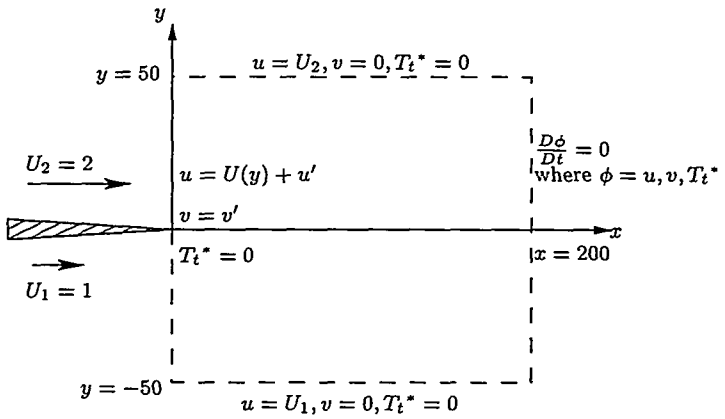

Figure 1: Schematic Diagram of Calculation Domain and Boundary Conditions

The governing equations for flow field are mass conservation, and unsteady Navier-Stokes equations. The present study assumes an incompressible and constant property fluid. The governing equations are written using the indicial notation as follows:

$$\frac{\partial u_i}{\partial x_i} = 0 \tag{1}$$

$$\frac{\partial u_i}{\partial t} + u_j \frac{\partial u_i}{\partial x_j} = -\frac{\partial p}{\partial x_i} + \frac{1}{Re_{\delta_o}} \frac{\partial}{\partial x_j}\left(\frac{\partial u_i}{\partial x_j} + \frac{\partial u_j}{\partial x_i}\right) \tag{2}$$

where u_i is i-th component of velocity. For convenience, u_1 is sometimes denoted by u, and u_2 by v. All variables are non-dimensionalized using a half the initial shear layer thickness δ_o, and the velocity difference ($\Delta U = U_2 - U_1$). The pressure (p) is normalized by $\rho \Delta U^2$. The Reynolds number (Re_{δ_o}) is based on δ_o and ΔU.

The governing equation for temperature field is total energy conservation equation. Reduced total energy equation with the assumption of non-conducting fluid is shown in Equation (3).

$$\frac{\partial T_t^*}{\partial t} + u_j \frac{\partial T_t^*}{\partial x_j} = \frac{\partial p}{\partial t} \tag{3}$$

where T_t^* is non-dimensional total temperature which is normalized with total temperature at the inlet T_{to} and two times of dynamic temperature $\Delta U^2/c_p$ such as $\frac{T_t - T_{to}}{\Delta U^2/c_p}$. For convenience, superscript $*$ is dropped after this.

A numerical algorithm using equal-order linear finite element and fractional four-step method is used to solve Equation (1), (2), and (3) simultaneously. Detailed discretized formulation of Equation (1) and (2) can be found in [10].

The discretized formulation of Equation (3) in time is obtained by the fractional step method, and written in Equation (4).

$$\frac{{T_t}^{n+1} - {T_t}^n}{\Delta t} + \frac{1}{2}({T_t}^{n+1}{u_j}^{n+1} + {T_t}^n{u_j}^n)_{,j} = \frac{1}{2}(p^{n+1} - p^{n-1}) \tag{4}$$

where Δt is the time increment, ',' represents spatial derivatives, and superscript n denotes the time step. The total-energy equation is discretized in space using the equal-order linear finite element method. The weak form of Equation (3) is obtained by multiplying it by a weighting function and integrating over the spatial domain (Ω) of the problem. By manipulating the integration with divergence theorem, the weak form is reduced as follows;

$$\int_\Omega w\left(\frac{\partial T_t}{\partial t} + u_j \frac{\partial T_t}{\partial x_j} - \frac{\partial p}{\partial t}\right) d\Omega = 0 \tag{5}$$

All variables are represented with variables at each node by the linear interpolation function:

$$\begin{aligned} u^e &= \sum_{k=1}^{4} N_k {u^e}_k, & v^e &= \sum_{k=1}^{4} N_k {v^e}_k \\ p^e &= \sum_{k=1}^{4} N_k {p^e}_k, & {T_t}^e &= \sum_{k=1}^{4} N_k {T_t^e}_{,k} \end{aligned} \tag{6}$$

where u_e is the velocity in x direction at element e, N_k is the interpolation function, and k is the number of the node in element e. Inserting Equation (6) into Equation (5), and integrating with respect to time by Equation (4) gives a linear algebraic equation at each node. The whole set of equations can be solved with the known u^e,v^e, and p^e.

A grid of 100 in x by 50 in y is used with $U_1 = 1$, and $U_2 = 2$. The Reynolds number (Re_{δ_o}) is 100 for all numerical simulation. All data is collected after all the initial field is

washed through the calculation domain.

The boundary conditions on each boundary of the calculation domain are shown in Figure 1. At the inlet plane ($x = 0$), a hyperbolic tangent profile with a very thin initial shear layer is employed for the velocity. In an actual shear layer, the velocity profile immediately downstream of the splitter plate is wake-like due to the existence of the plate. However, the velocity profile is quickly assumed as a tanh-like shape, because of intensive momentum diffusion across the shear layer caused by the large velocity gradient in the spanwise direction. Consequently, the hyperbolic tangent profile assumption is reasonable.

To simulate experimental flow conditions, small disturbances are introduced at the inlet plane. The disturbances are obtained from stability analysis of inviscid flow with the same inlet velocity profiles. Most unstable frequency and its two sub-harmonic frequencies are selected as the frequencies of the disturbance. The magnitude of each disturbance is 0.03 so that the turbulence intensity at the inlet plane is less than 2%. The boundary condition of u is written in Equation (7).

$$u(0, y, t) = \frac{1}{2}\left[\frac{U_2 - U_1}{U_2 + U_1} + \tanh(2y)\right] + 0.03 \sum_{j=1}^{3} \tilde{u_j}(y, t) e^{-i\omega_j t} \tag{7}$$

Similar disturbances are also introduced in the y direction. For temperature, uniform total temperature is assumed.

At the outlet plane, a convective boundary condition is used. The convective boundary condition is a suitable condition for handling a vortex passing across a boundary. The detailed validity of this boundary condition can be found in [10, 11]. Boundary conditions at the other two boundaries are assumed to be the same as the free stream.

RESULTS AND DISCUSSION

Vorticity is a convenient variable to describe the motion of a vortex in a flow field. The vorticity (ω_z) is defined as,

$$\omega_z = \frac{\partial v}{\partial x} - \frac{\partial u}{\partial y} \tag{8}$$

In Figure 2, the vorticity distribution at different times are shown. The disturbance applied at the inlet plane starts growing and rolls up into vortices. The interaction between the vortices is observed. Near the inlet plane, very small size of vortices are formed, and merge with neighboring ones. The merged vortex moves downstream, and combines with another merged one. This interaction was observed in many experimental studies [12, 13].

Instantaneous pressure and temperature distributions are presented in Figure 3. It shows that the formation of vortices distorts the pressure fields. Pressure near the center of vortices is lower than surrounding, and has local minimum value. Between the minimum points, local maximum pressure points exist.

Instantaneous total temperature distribution shown in Figure 3 (b) indicates the instantaneous energy separation. The locations of the separation nearly match with those of vortex

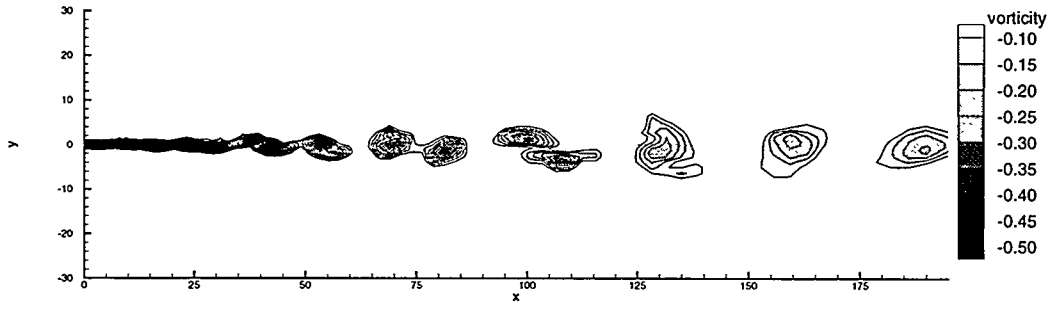

(a) when t=250

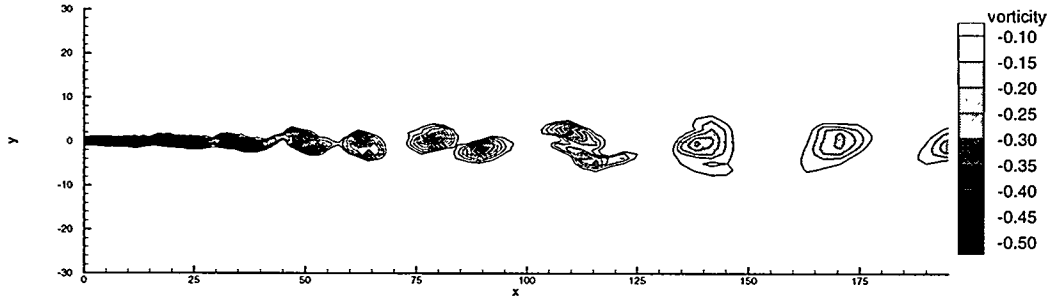

(b) when t=275

Figure 2: Instantaneous Vorticity (ω_z) Distribution

center. This verifies that the pressure fluctuation due to the motion of vortex is the cause of energy separation. The temperature distribution is asymmetric, which is different from the results of inviscid calculation [9]. The maximum amount of the separation is obtained around $x = 145$. After that location, the energy separation starts to weaken. This should be caused by the effect of viscosity. The vortices generated from the initial disturbances are dissipated due to the viscosity of fluid as they moves downstream.

With the observation above, the mechanism of instantaneous energy separation can be explained as follows. Since the vortex is moving with a certain velocity, the distortion in pressure field is also moving. Due to the motion, fluid at the front-half of vortex experiences negative $\frac{\partial p}{\partial t}$ (i.e. do the pressure work to surrounding fluid), and fluid at the rear-half does positive $\frac{\partial p}{\partial t}$ (i.e. the pressure work done by surrounding fluid is added). Therefore, fluid loses energy passing through the front-half of the vortex, and gains energy through the rear-half.

In Figure 4, the pressure around vortices and total temperature variations of fluid particles are illustrated. Thickness of the line represents the pressure at that point, and color denotes the total temperature of the fluid. A fluid particle which enters flow field from $y > 0$, is entrained into shear layer through the front-half of vortices. Along this path, the fluid particle lose energy and reach its local minimum temperature after passing where $y = 0$.

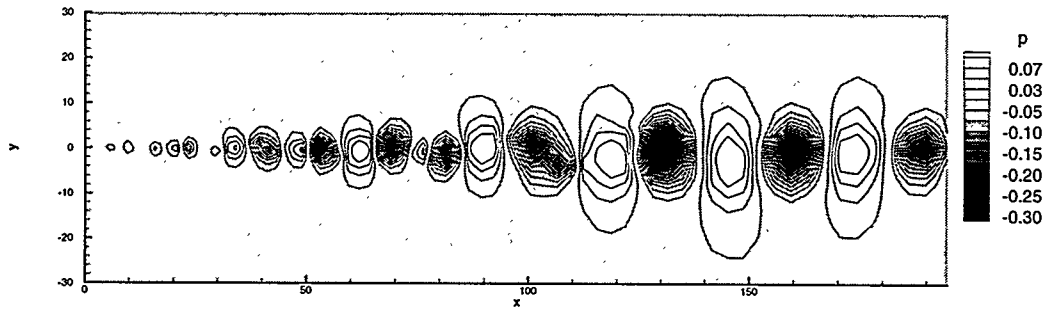

(a) Instantaneous pressure distribution when t=250

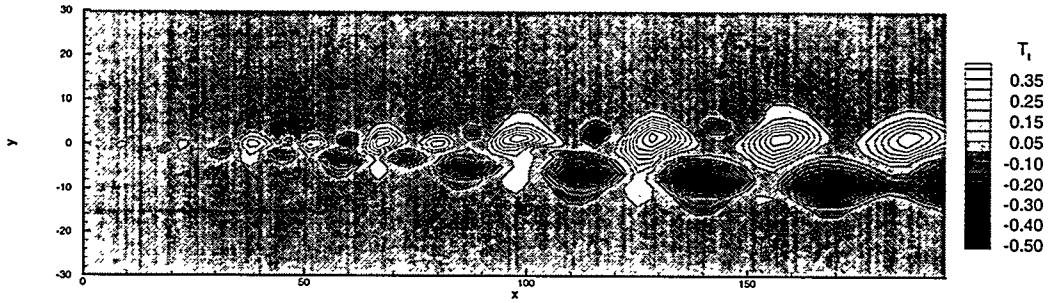

(b) Instantaneous total temperature distribution when t=250

Figure 3: Instantaneous Pressure and Total Temperature Distribution

After that, the particle moves upward by the motion of vortex through the rear-half. Along this path, the particle gain energy and return to nearly its initial total temperature.

Even though a fluid particle from $y < 0$ is entrained similarly, the different sequence of entrainment causes reverse total temperature distribution. Initially the particle is entrained through the rear-half of vortex. Due to the entrainment through this path, the particle gains energy first, and reach local maximum temperature. These local maximum and minimum total temperature are believed to contribute to energy separation.

CONCLUSION

A numerical study on instantaneous mechanism of energy separation was performed. A computational code to simulate unsteady two dimensional flow and total temperature field has been developed. Physical explanation based on the results of numerical analysis was proposed. The conclusions of the present research can be summarized as follows:

1. Numerical simulation shows the instantaneous mechanism of energy separation due to the pressure fluctuations.

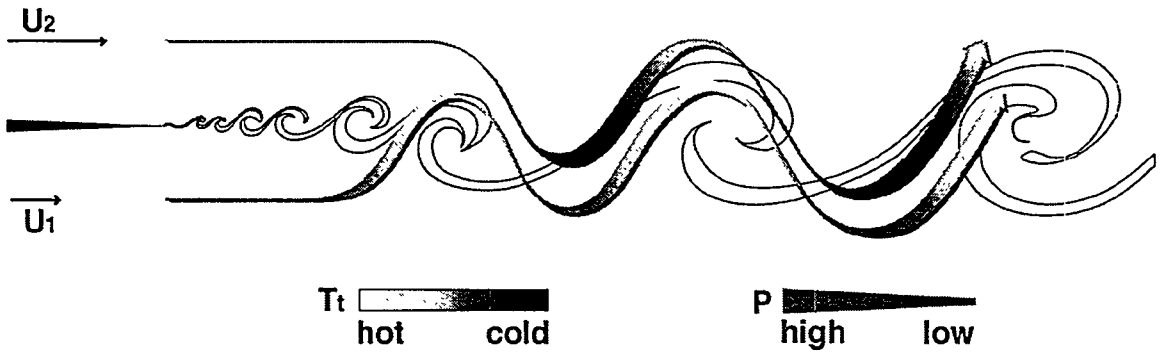

Figure 4: Pressure and Total Temperature Variation along Pathlines in a Shear Layer

2. Motion of vortices in shear layer induces pressure fluctuations in flow fields. The pressure fluctuations induced by the vortex motion cause the energy separation.

3. Instantaneous total temperature distribution is asymmetric. This should be caused by asymmetric entrainment of fluid from two sides of shear layer.

An experimental study to measure instantaneous total temperature in shear layer of jet flows is in progress by the authors. The experimental results will provide useful data to help to understand the instantaneous mechanism of energy separation, and can verify the results of the numerical simulation.

ACKNOWLEDGMENTS

The authors would like to thank the U.S. Department of Energy for the support of this work. We wish to thank Dr. H. G. Choi, and Dr. S. Garrick for their comments and discussion on the computational code development. The present study was carried out at the University of Minnesota Supercomputing Institute.

REFERENCES

[1] E. Eckert and W. Weise, "Messungen der Temperaturverteilumg auf der Overfläche schnell angeströmter unberheizter Körper," *Jahrbuch 1940 der deutschen Luftfahrtforschung* **II**, 25 (1940).

[2] E. Eckert and O. Drewitz, "Die Berechnung des Temperaturefeldes in der Laminaren Grenzschichtschnell Angeströmter Unbeheizter Körper," *Luftfahrtforschung* **19**, 189 (1941).

[3] R. J. Goldstein, A. I. Behbahani and K. K. Heppelman, "Streamwise Distribution of the Recovery Factor and the Local Heat Transfer Coefficient to an Impinging Circular Air Jet," *Int. J. Heat Mass Transfer* **29**, 1227 (1986).

[4] W. S. Seol, *Energy Separation in a Jet Flow*, Ph.D. thesis, University of Minnesota, Minneapolis (1993).

[5] M. Kurosaka, J. B. Gertz, J. E. Graham, J. R. Goodman, P. Sundaram, W. C. Riner, H. Kuroda and W. L. Hankey, "Energy Separation in a Vortex Street," *J. Fluid Mech.* **178**, 1 (1987).

[6] J. J. O'Callaghan and M. Kurosaka, "Vortex-Induced Energy Separation in Shear Flows," *AIAA Journal* **31**, 1157 (1993).

[7] E. R. G. Eckert, "Cross Transport of Energy in Fluid Streams," *Wärme-und Stoffübertranung* **21**, 73 (1987).

[8] W. F. Ng, W. M. Chakroun and M. Kurosaka, "Time-Resolved Measurements of Total Temperature and Pressure in the Vortex Street behind a Cylinder," *Phys. Fluids A* **2**, 971 (1990).

[9] M. D. Fox, M. Kurosaka, L. Hedges and K. Hirano, "The Influence of Vortical Structure on Thermal Fields of Jets," *J. Fluid Mech.* **255**, 447 (1993).

[10] H. G. Choi, H. Choi and J. Y. Yoo, "A Fractional Four-Step Finite Element Formulation of The Unsteady Incompressible Navier-Stokes Equations Using SUPG and Linear Equal-Order Element Methods," *Comput. Methods Appl. Mech. Engrg.* **143**, 333 (1997).

[11] P. M. Gresho, "Some Current CFD Issues Relevant to the Incompressible Navier-Stokes Equations," *Comput. Methods Appl. Mech. Engr.* **87**, 201 (1991).

[12] A. K. M. F. Hussain and K. B. M. Q. Zaman, "Vortex Pairing in a Circular Jet under Controlled Excitation. Part2 - Coherent Structure Dynamics," *J. Fluid Mech.* **101**, 493 (1980).

[13] A. K. M. F. Hussain, "Coherent Sturctures and Turbulence," *J. Fluid Mech.* **173**, 303 (1986).

DYNAMIC HOLOGRAPHIC LOCK-IN IMAGING OF ULTRASONIC WAVES

K. L. Telschow, V. A. Deason

Idaho National Engineering and Environmental Laboratory
Lockheed Martin Idaho Technologies Co.
Idaho Falls, ID 83415-2209

S. K. Datta

Department of Mechanical Engineering
University of Colorado
Boulder, CO 80309-0427

ABSTRACT

A laser imaging approach is presented that utilizes the adaptive property of photorefractive materials to produce a real-time measurement of ultrasonic traveling wave surface displacement and phase in all planar directions simultaneously without scanning. The imaging method performs optical lock-in operation. A single antisymmetric Lamb wave mode image produces direct quantitative determination of the phase velocity in all planar directions showing plate stiffness anisotropy. Excellent agreement was obtained with modeling calculations of the phase velocity in all planar directions for an anisotropic sheet material. The approach functions with diffusely scattering surfaces, subnanometer motions and at frequencies from Hz to GHz.

INTRODUCTION

A powerful method for imaging ultrasonic motion has been developed at the INEEL that utilizes the photorefractive effect in optically nonlinear materials to perform adaptive interferometry.[1,2] Optical interference is developed within a photorefractive material with this technique and the output is an optical image whose intensity distribution is directly proportional to the surface vibration amplitude, for small ultrasonic displacements. Utilizing this approach, no postprocessing of the data recorded by a video camera is required to produce images of the surface vibration amplitude over large areas. Application of this approach, referred to as the *INEEL Laser Ultrasonic Camera*, to imaging of standing wave resonant motion in plates has been previously described.[3,4,5] This paper describes optical lock-in operation of this imaging method by recording the nonstationary waveform of a traveling Lamb wave in a plate.[6]

PHOTOREFRACTIVITY BACKGROUND

Photorefractivity refers to that process where optical excitation and transport of charge carriers within select nonlinear optical materials produces a diffraction grating or hologram from the interference pattern developed inside the material. A spatial and temporal charge distribution results in the photorefractive material that reflects the phase information impressed onto an optical signal beam (e.g. by a vibrating surface). The INEEL method records the photorefractive grating produced at a fixed beat frequency between the phase modulated signal and reference beams. It can directly measure vibration amplitude and phase with a response proportional to the Bessel function of order one, providing a linear output for small amplitudes. The method accommodates rough surfaces, exhibits a flat frequency response above the photorefractive response cutoff frequency, and can be used for detecting both standing and traveling waves.

EXPERIMENTAL METHOD

The experimental setup for vibration detection is shown in Figure 1. A solid state laser source at 532 nm was split into two legs forming the signal and reference beams. The signal beam was reflected off traveling waves produced at the surface of a plate driven at its center by a continuously excited piezoelectric transducer. The traveling wave motion occurring on the plate surface produced a phase modulation δ_{sig} of the signal beam. The reference beam was phase modulated by an electro-optic modulator at a fixed modulation depth δ_{ref}. The modulated beams were combined and interfered inside a Bismuth Silicon Oxide (BSO) photorefractive crystal with operation in the diffusive regime. In the four-wave mixing configuration, the reference beam was reflected back into the crystal along a counter-propagating path that matched the Bragg angle of the photorefractive grating in the medium. The vibration modulated phase grating was read out by

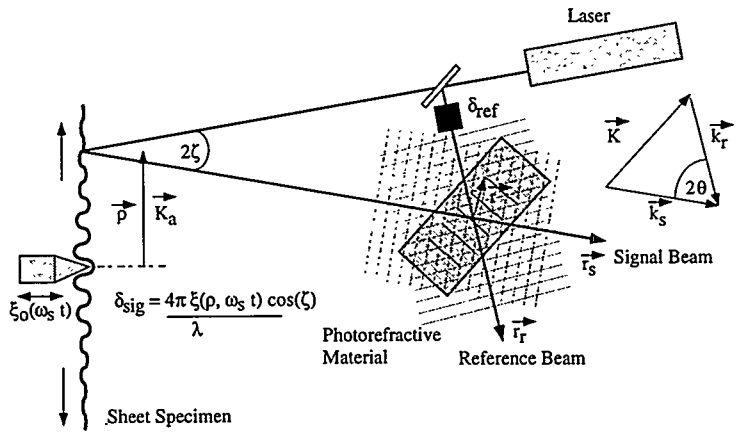

Figure 1. Optical Lock-in Ultrasonic Imaging Setup.

the resulting scattered wave that propagated backward along the signal beam leg and was detected by deflecting it with a beamsplitter (not shown) toward a photodetector or a video camera.

FLEXURAL WAVE DISPLACEMENT DISTRIBUTION

The lock-in mechanism that allows recording of ultrasonic wave displacements can be illustrated by considering a traveling flexural wave in a plate[7]. The displacement normal to the plate surface of a wave from an oscillating point excitation force F_0, for wavelengths larger than the plate thickness, is given by[8] $\xi(\rho,t) = \mathrm{Re}(i\xi_0\,[H_0^1(k_a\rho) - H_0^1(ik_a\rho)]e^{-i(\omega_s t+\varphi_s)})$ where $\xi_0 \equiv \frac{F_0}{8\omega\sqrt{D\sigma}}$, $k_a = \frac{2\pi}{\lambda_a}$ and $H_0^1(x)$ is the Hankel function of order zero representing a wave traveling outward from the origin. $D \equiv \frac{Eh^3}{12(1-s^2)}$ is the bending stiffness of the plate, $\sigma \equiv \rho_m h$ the mass density per unit area, ρ_m = the mass density, s = Poisson's ratio, E = Young's modulus and h = the plate thickness. The 2-dimensional spatial Fourier transform yields poles at the propagation wavevector $k_a^4 \equiv \frac{\sigma\omega^2}{D}$ as $\tilde{\xi}_\rho(q) = \frac{F_0}{D}\left[\frac{1}{(q^2-k_a^2)(q^2+k_a^2)}\right]$.

OPTICAL LOCK-IN TRAVELING WAVE DETECTION

The method by which the optical lock-in process demodulates the phase information can be illustrated by considering the four-wave mixing detection process. The Hankel function can be

written as $H_0^1(x) = h_0(x)\, e^{i(x-\frac{\pi}{4})}$ to configure the optical phase shift of the signal beam as $\Phi_{sig}(\rho,t) = \frac{4\pi\xi(\rho,t)}{\lambda} = \frac{4\pi}{\lambda}\xi_0 |h(k_a\rho)| \sin(\omega_s t + \varphi_s - k_a\rho + \frac{\pi}{4} - \Phi_a)$, where $|h(k_a\rho)| e^{i\Phi_a} \equiv h_0(k_a\rho) - h_0(ik_a\rho)e^{-k_a\rho(1+i)}$. Using the relation $e^{ix\sin(\theta)} = \sum_{n=-\infty}^{n=\infty} J_n(x)e^{in\theta}$ and $\Phi_{sig0} = \frac{4\pi\xi_0}{\lambda}$, the optical signal beam amplitude becomes

$A_s(r,t) = A_{s0} e^{i(\vec{k}_s\cdot\vec{R}_s - 2\pi\nu t)} \sum_{n=-\infty}^{n=\infty} J_n(\delta_{sig0})\, e^{in(\omega_s t + \varphi_s - k_a\rho + \frac{\pi}{4} - \Phi_a)}$ where $\vec{R}_s = \vec{r} + \vec{r}_s$, $\delta_{sig0} = \Phi_{sig0}|h(k_a\rho)|$ and ν is the laser optical frequency. The reference beam is similarly phase modulated by an electro-optic modulator (EOM) according to $\delta_{ref} = \delta_{ref0}\sin(\omega_r t + \varphi_r)$. $\delta_{sig0}, \delta_{ref0}$ are the magnitudes, ω_s, ω_r are the modulation frequencies and $\vec{r}_s, \vec{r}_r$ are the standoff distances and φ_s, φ_r are the modulation phases imposed by the specimen (signal) and the electro-optic modulator (reference), respectively.

Interference inside the crystal produces a spatially and temporally modulated intensity pattern with $\vec{K} = \vec{k}_s - \vec{k}_r$ the grating wavevector and $\Sigma = \vec{k}_s\cdot\vec{r}_s - \vec{k}_r\cdot\vec{r}_r$ accounting for path length differences between the two beams. The interference intensity distribution within the crystal generates a corresponding space charge electric field distribution. The dynamic behavior of this field is controlled by the charge carrier mobility and trapping that produces, in the diffusive operation regime, a single relaxation time response given by $\frac{\partial E_{sc}}{\partial t} + \frac{E_{sc}}{\tau} = \frac{iE_q}{\tau}\frac{2A_s\cdot A_r^*}{I_0}$, where τ, the material response time and E_q, are controlled by properties of the photorefractive material and the fringe spacing. In the above configuration, the photorefractive crystal acts as a mixing and low pass filtering element providing the benefits of lock-in detection. Therefore the space charge field responds to slowly varying phase modulations occurring within the material response time allowing only the terms around the difference frequency $\Omega\tau \le 1$ to be important, assuming $\Omega << \omega_{s,r}$. With $\Omega = \omega_r - \omega_s$, $\Phi = \varphi_r - \varphi_s$, $\tan(\psi_n) = n\Omega\tau$, and $\chi(\rho) = (k_a\rho - \frac{\pi}{4} + \Phi_a)$, the resultant space charge field becomes $E_{sc}(\vec{r},t) = E_q M f(\delta_{sig0}(\rho),\chi(\rho);t)\sin(\vec{K}\cdot\vec{r} + \Sigma)$, with

$$f(\delta_{sig0}(\rho),\chi(\rho);t) = \left[\begin{array}{l} J_0(\delta_{ref0})J_0(\delta_{sig0}(\rho)) + \\ 2J_1(\delta_{ref0})J_1(\delta_{sig0}(\rho))\dfrac{\cos(\Omega t + \Phi - \chi(\rho) - \psi_1)}{\sqrt{1+\Omega^2\tau^2}} + \ldots \end{array}\right]$$ where J_n is the Bessel function of the first kind.

The space-charge field modulates the local refractive index through the linear electro-optic effect. This effect creates a diffraction grating within the crystal that contains the low frequency phase information desired. The magnitude of the index of refraction grating produced is

$n_1 = \frac{n_0^3 r_{41} E_{sc}}{2}$, where n_0 is the average refractive index of the medium, r_{41} is the effective, orientation-dependent electro-optic coefficient. The diffraction efficiency of the grating is determined by the wave coupling constant $\zeta \equiv \left|\frac{\pi n_1 L}{\lambda \cos\theta}\right| = \frac{\Gamma L}{2} M f(\delta_{sig0}, \chi; t)$ where L is the interaction length, $\Gamma \equiv \frac{\pi n_0^3 r_{41} E_q}{\lambda \cos\theta}$ is the quadrature phase grating two-wave mixing coupling constant, λ is the source wavelength, and 2θ is the angle between the mixing waves.

In the four-wave mixing arrangement, the reference beam that passes through the crystal is reflected back into the crystal and diffracts from the photoinduced grating retracing the signal beam path. In the undepleted pump approximation, the diffracted (conjugate) beam intensity is given by $I_4 = I_3 e^{-\alpha L/\cos\theta} |\sin\zeta|^2$, where I_3 is the back-propagated reference beam intensity and α is the material absorption coefficient[9]. The refractive index modulation amplitude generated by the mixing process is generally small, so that $\zeta << 1$, *and* $\sin(\zeta) \approx \zeta$. The first time varying or AC term in the intensity of the diffracted beam is given by $I_4 \propto \left(\frac{\Gamma L}{2}\right)^2 M^2 \left[\frac{4 J_0(\delta_{ref0}) J_1(\delta_{ref0})}{\sqrt{1+\Omega^2\tau^2}}\right] J_0(\delta_{sig0}) J_1(\delta_{sig0}) \cos(\Omega t + \Phi - \chi(\rho) - \psi)$ where $\tan(\psi) = \Omega\tau$. This result shows that the magnitude and phase of the traveling wave have been placed into the arguments of the Bessel functions for the magnitude and as the phase of a low frequency AC signal. The resultant measured intensity, for small traveling wave displacement, is $I_{AC} \propto \frac{\delta_{sig0}}{2} \cos(\Omega t + \Phi - \chi(\rho) - \psi) \quad \propto \frac{4\pi\xi(\rho, \Omega t + \vartheta)}{\lambda}, \quad \vartheta = \Phi - \psi(\Omega\tau) + \frac{\pi}{2}$. The imaging approach provides a measure of both the traveling wave amplitude and phase for small amplitudes relative to the optical wavelength, ($\frac{4\pi\xi(\rho,t)}{\lambda} << 1$). The maximum detectable signal amplitude occurs at a phase shift of about one radian, corresponding to a traveling wave amplitude of about 45 nm for a probe wavelength of 532 nm.

OPTICAL LOCK-IN IMAGING

Since optical interference and the photorefractive effect occur throughout the photorefractive crystal, lock-in detection of the vibration over many points on the surface of the plate can be performed simultaneously. The volume character of the photorefractive process creates a grating distribution that locally records the phase modulation measured from each point of the specimen surface as long as the surface is accurately represented within the photorefractive crystal. The output beam intensity can then be measured by a CCD camera. Each pixel records the local intensity from a point on the specimen producing an output proportional to that point's

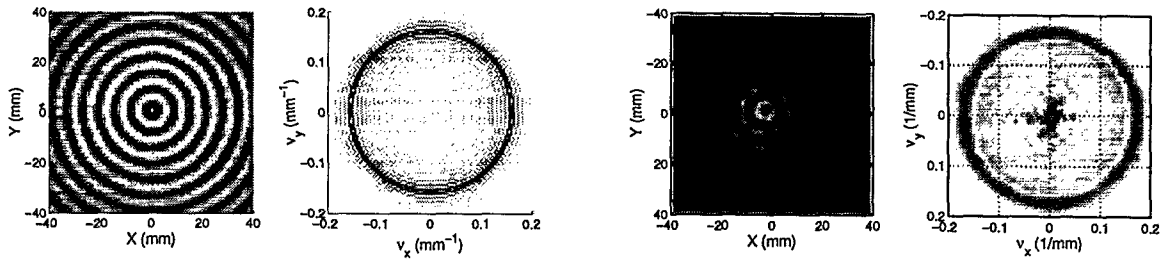

Figure 2: Calculated (left) and Measured (right) Traveling Wave Displacements and Magnitude of the 2-D FFT for the Nickel Plate at 30.0 kHz.

displacement. Even a diffusely reflecting surface can be measured if the surface is adequately imaged inside the photorefractive crystal by suitable optics.

Figure 2 shows an image of a traveling flexural wave in a 0.125 mm thick nickel plate at 30 kHz with $E = 204\ GPa$, $s = 0.31$, $\rho_m = 8.9\ g/cm^3$. The expected circular wavefronts due to the isotropic microstructure of the nickel plate are clearly defined and the ultrasonic displacement phase is readily distinguishable. The figure shows single frame image data. The entire pattern can be made to change its phase continuously at the frequency, Ω, from about 1–30 Hz, so that the appearance is that of waves emanating from the center and traveling outward. This is physically equivalent to the actual traveling wave motion except that viewing of the wave has been slowed to a much smaller observation frequency that is held constant and independent of the actual wave frequency. The photorefractive process yields a true picture of the actual wave vertical displacement motion and requires no additional processing for the images of Figure 2.

The magnitude of the Fourier transform of the traveling wave displacement shows real poles at the wavevector for the traveling wave and imaginary poles of the same magnitude that contribute to satisfy the boundary conditions. Therefore, the Fourier transform image of the traveling wave displacement image is a single ring at the wavevector delineating the propagating mode. Figure 2 shows images of the calculations and measurements of the traveling wave displacements. Also shown are images of the magnitudes of the Fourier transforms. A strong response is seen as a ring at the propagating wavevector that can be immediately measured to quantitatively show the elastic constants and the isotropic character of the plate. This analysis procedure provides considerable information about the plate in one simple image.

ANISOTROPIC MATERIAL MEASUREMENTS

If the specimen is elastically anisotropic, then the wave speed varies with the propagation direction. Figure 3 shows this type of behavior for traveling waves in a sheet of copy paper. The

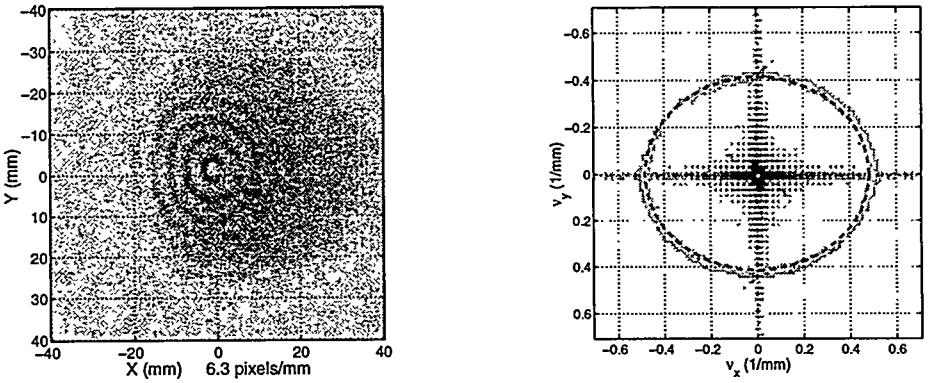

Figure 3: (left) INEEL Camera Image of Ultrasonic Waves In Paper, (right) Magnitude of the Fourier Transform of the Camera Image and Calculational Result (dashed lines).

paper sheet had its fibers aligned approximately along the vertical direction. The highly oblong wavefront pattern shows the anisotropy immediately. Modeling calculation of the elastic wave anisotropy for all planar angles has been performed from independent measurements of the elastic constant matrix for this paper material. Comparison with the image data provides direct measurement of the crystallographic axes orientation present in the material. Very good agreement between the calculations and the measurements can be seen at all directions in figure 3 and at all frequencies as shown in figure 4. Coupled with detailed modeling of this type, the *INEEL Laser Ultrasonic Camera* approach provides the an important step for developing a means of determining arbitrary orientations of anisotropic materials from wave images using data from all planar directions simultaneously.

CONCLUSIONS

An imaging optical lock-in traveling wave measurement method has been described. Direct two-dimensional surface images of the traveling wave were obtained by expanding the collection optics and imaging the output beam from the photorefractive material. These images showed the ultrasonic wavelength and wavefront shape in all planar directions and provided a quantitative method for obtaining the elastic stiffness of sheet materials, as illustrated for an isotropic nickel plate and an anisotropic sheet of paper. The method is capable of flat frequency response over a wide range above the reciprocal of the photorefractive time constant and is applicable to imaging the ultrasonic motion of surfaces with rough, diffusely reflecting finishes. Coupled with detailed modeling of anisotropic elastic properties of materials, imaging provides a powerful technique for microstructure measurement and analysis.

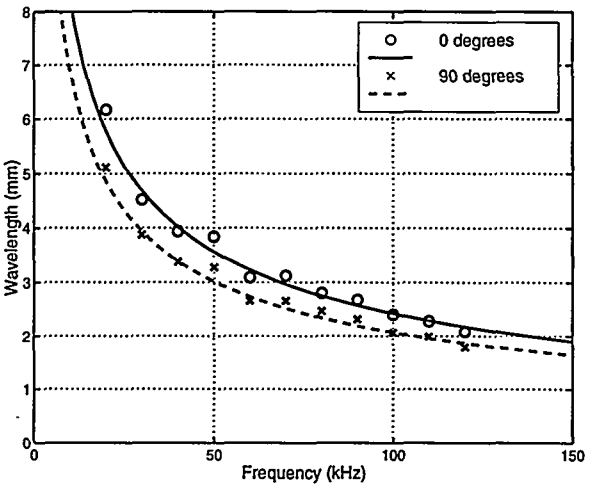

Figure 4. Measured and Calculated Wavelengths

ACKNOWLEDGMENTS

The authors thank S. M. Watson and R. S. Schley for experimental help, A. Jonas Niklasson for the modeling calculations, and Dr. J. Gerhartstein and Dr. P. Brodeur of the Institute of Paper Science and Technology, Atlanta, GA, for the elastic constant matrix for the paper sample. This work was sponsored by the U.S. Department of Energy, Office of Energy Research, Office of Basic Energy Sciences, Engineering Research and the INEEL Laboratory Directed Research & Development program under DOE Idaho Operations Office Contract DE-AC07-94ID13223.

REFERENCES

1 P. Yeh, *Introduction to Photorefractive Nonlinear Optics*, (John Wiley, New York, 1993).

2 S. I. Stepanov, *International Trends in Optics*, (Academic Press, New York, 1991) Ch. 9.

3 T. C. Chatters and K. L. Telschow, *Review of Progress in QNDE*, Vol. 15B, Eds. D.O. Thompson and D. E. Chimenti, (Plenum Press, New York, 1996) pp. 2,165–2,171.

4 T. C. Hale and K. Telschow, Appl. Phys. Lett. 69, 2,632–2,634 (1996).

5 T. C. Hale, K. L. Telschow, and V. A. Deason, Applied Optics, 111, 8,248–8,258 (1997).

6 K. L. Telschow, V. A. Deason, R. S. Schley and S. M. Watson, *Review of Progress in QNDE*, Vol. 18, Eds. D.O. Thompson and D. E. Chimenti, (Plenum Press, New York, 1999) to be published.

7 K.L. Telschow, V. A. Deason, R. S. Schley and S. M. Watson, "Direct Imaging of Lamb Waves in Plates using Photorefractive Dynamic Holography," to be published.

8 P. M. Morse and K. U. Ingard, *Theoretical Acoustics*, (McGraw-Hill, New York, 1968) 219.

9 H. Kogelnik, Bell System Technical Journal 48, 2,909–2,947 (1969).

MECHANICAL BEHAVIOR AND ULTRASONIC CHARACTERIZATION OF DUCTILE/BRITTLE LAYERED MATERIAL SYSTEMS

S. K. Datta, M. L. Dunn, R. Sesselmann and J. Niklasson

Department of Mechanical Engineering
University of Colorado
Boulder, Colorado 80309

ABSTRACT

We attempt to provide a mechanistic understanding of the cracking phenomena in brittle/ductile layered materials under axial and transverse mechanical loading, and an ultrasonic framework within which to characterize their mechanical properties and integrity. The former consists of models and measurements of cracking in a brittle layer sandwiched between two ductile layers subjected to axial tension and transverse compression. The latter consists of measurement models that can be applied inversely when coupled with ultrasonic measurements to determine mechanical properties of both individual layers and the layered system as a whole.

INTRODUCTION

Considerable effort is currently being directed toward the development of long-length high-T_c superconducting cables. Regardless of the actual materials or fabrication technologies, the cables are composites consisting of a brittle superconductor phase and a ductile metal phase. While in theory high-T_c superconductors have the potential to generate extremely large magnetic fields due to their high upper critical field, in practice the electromechanical response of the conductor to large Lorentz forces dictates the magnetic field limits. Layered superconducting cables are often wound in magnets and in such a configuration the layered structure is subjected to thermomechanical loading that arises from at least three sources: i) fabrication where the tape is wound under a pretension into a cylindrical shape; ii) thermal expansion mismatch between the layers; and iii) magnetic fields. The latter lead to tensile hoop and compressive transverse stresses on the conductor. The design of superconducting magnets requires a solid understanding of the role of these stresses on electromechanical failure of the superconductor. In high-T_c materials, the electromechanical failure mechanism appears to be transverse cracking that occurs in the brittle superconducting layer (Ekin, 1992; Salib and Vipulanandan, 1997). This results in an *irreversible* dependence of critical current/field on stress/strain; an example is shown in Fig.

1a (from Ekin et al., 1992). More recently, critical current degradation has been observed under transverse loading (Ekin, 1998).

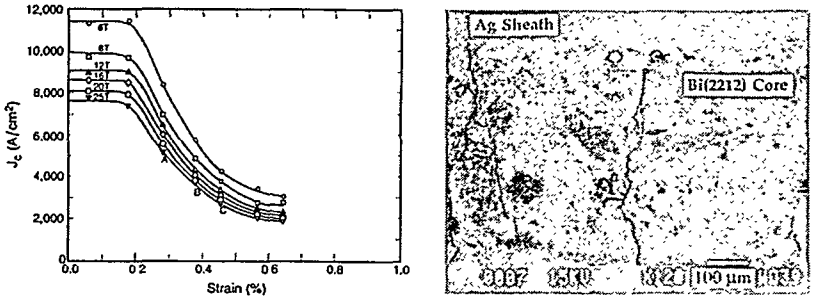

Fig. 1 (a) Critical current vs. applied axial strain for a Bi(2212)/Ag superconducting tape, and (b) microstructure of the conductor showing the development of transverse crack arrays (from Ekin et al., 1992).

There exists an extensive body of literature concerned with cracking in layered material systems and a complete review is far beyond the scope of this work. Comprehensive reviews of the subject are given by Hutchinson and Suo (1991) and Evans and Hutchinson (1995). The mechanistic understanding of layer cracking now seems to exist, and is well-articulated by Hutchinson and Suo (1991). The failure mode of interest here has been referred to as crack tunneling or channeling (or crazing in the case of film/substrate systems), and the concept of a steady-state energy release rate for crack channeling has emerged as an important and powerful approach to describe the phenomena (Ho and Suo, 1991; Beuth, 1992). The basic idea is to focus attention on the final cracked state (a crack that has fully channeled across the brittle layer) and not on the details of the complicated initiation phenomena. Complete details of the steady-state cracking concept are given by Hutchinson and Suo (1991) and references therein. Motivated by the success of this concept to explain many problems regarding crack channeling, we obtain steady-state cracking solutions for cracks in a sandwich layer subjected to transverse compression.

The characterization of the mechanical behavior of such layered systems presents a significant challenge. Ultrasonic nondestructive evaluation (NDE) techniques have found wide use for quantitative characterization of mechanical properties and for detection of cracks and delamination in layered plates. Their use, however, requires a clear understanding of wave propagation in anisotropic and layered plates. In this paper, we focus on guided waves in a plate with superconducting layers. Investigation of in-situ mechanical behavior and properties of thin superconducting layers has been limited. The properties are highly dependent on the manufacturing processes, internal and external stress fields, interface properties, porosity, and the extent of possible cracking in the brittle layers. In order to model these different effects accurately, it is necessary to understand the basic problem of guided wave propagation in a three-layered thin plate where the brittle layers are on either the outside or inside. Since the superconductor layer can be quite thin compared to the overall thickness of the plate, a model study is presented here for this particular case and exact and approximate solutions are presented. To approximate the thin layer we expand the fields in the (small) thickness and obtain approximations by truncation of the infinite series. This approach has been taken by Bövik (1994, 1996) for isotropic materials. Here we extend the approach of Bövik to anisotropic coatings for the three-dimensional case.

ULTRASONIC CHARACTERIZATION OF LAYERED SYSTEMS

Wave propagation in a layered plate with orthotropic layers having a common symmetry axis perpendicular to the layers has been studied by Karunasena *et al.* (1991). Guided waves in a layered plate with layers of different anisotropic properties have also received some attention. This problem is important for ultrasonic characterization of layered bonded plates when the interface (interphase) bond (adhesive) properties are significantly different than the adjacent layers. In a recent paper, Shull *et al.* (1994) considered ultrasonic wave propagation in a layered plate with alternative layers of aluminum and adhesive formed by aramid fiber reinforced epoxy. Experimental observations and theoretical model results were presented. Plates having varying number of layers were considered. Here we present a theoretical analysis of ultrasonic wave propagation in a plate with anisotropic layers. The theoretical development is presented in a general form, followed by numerical results for the case of a three-layered plate. We present a combined stiffness and analytical method to calculate the guided wave modes in a layered anisotropic plate.

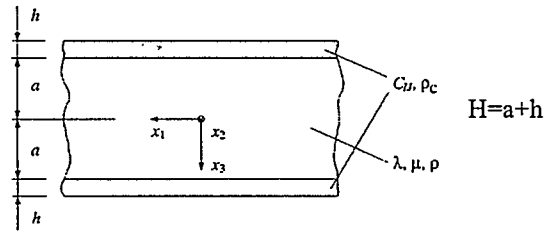

Figure 2. Geometry of the layered plate: x_3 is normal to the layering, x_1 is the wave propagation direction.

We consider time harmonic elastic waves in an infinite plate (Fig. 2) composed of perfectly bonded layers with distinct elastic properties and thickness. The two faces of the plate $x_3 = -H$ and $x_3 = H$ are traction free. In the stiffness method, each layer is divided into several sublayers so that the total number of sublayers through the thickness 2H is N. Let u_i denote the displacement components in the x_i directions. Consider the *i*th sublayer bounded by $x_3 = z_i$ and z_{i+1}. Within the *i*th sublayer we approximate the displacement components through the thickness as

$$\{u\} = [N]\{q\} \tag{1}$$

$$\{u\}^T = [u_1\ u_2\ u_3], \qquad \{q\}^T = [u_1^b\ u_2^b\ u_3^b\ u_1^m\ u_2^m\ u_3^m\ u_1^f\ u_2^f\ u_3^f] \tag{2}$$

In Eqs. (1)-(2), the generalized displacements u^b, u^m, and u^f are taken at the back (bottom), middle, and the front (top) nodal surfaces of the sublayer. The interpolation polynomials N_i are quadratic functions of position. Using Hamilton's principle, the governing equation for the entire plate can be expressed as:

$$-[K_1]\{Q\}'' + [K_2]\{Q\}' + [K_3]\{Q\} + [M]\{Q\} = \{F\} \tag{3}$$

where {Q} and {F} are vectors representing the nodal displacements and tractions applied at the interfaces of the plate. The matrices $[K_1]$, $[K_3]$, and [M] are symmetric, whereas $[K_2]$ is antisymmetric. Applying the Fourier transform to equation (3) with respect to x_1 (the

propagation direction) and assuming that the field variables have harmonic time dependence of the form exp(-jωt), we obtain

$$\{F\} = \left(k^2[K_1] + jk[K_2] + [K_3] - \omega^2[M]\right)\{Q\} \tag{4}$$

Setting {F}={0} yields a homogeneous system of equations describing the propagation of guided waves in the plate. For a nontrivial solution, the determinant of the resulting coefficient matrix must vanish. This condition yields the discretized form of the dispersion equation for guided waves propagating in the x_1-direction and can be solved for the eigenvalue ω for a given wavenumber k or for the eigenvalue k when ω is fixed. The stiffness method just described is applicable to generally anisotropic layers. For the special case of transverse isotropy, the dispersion equation can be derived in closed form. This is summarized in Datta *et al.* (1999).

When the outer layer thickness, h, is small compared to the inner layer, a simplified approximate solution can be obtained. We describe the method and results briefly here, but refer Niklasson *et al.*(1999) for complete details. We consider a thin anisotropic coating at $-h < x_3 < 0$ on a substrate at $x_3 > 0$. We assume that the thickness of the coating is small compared to the wavelengths and expand the traction through the thickness of the coating as

$$(\sigma_{j3})_{-h} = (\sigma_{j3})_0 - h(\partial_3\sigma_{j3})_0 + O(h^2) \tag{5}$$

where $\partial_j = \partial/\partial x_j$ and below $\partial_t = \partial/\partial t$ as well. By using the equations of motion in the coating, the boundary conditions at $x_3 = -h$, and the interface conditions at $x_3 = 0$, we arrive at the effective boundary condition

$$\hat{\mathbf{o}} + h(A_\sigma\hat{\mathbf{o}} + A_u\mathbf{u}) = O(h^2), \qquad x_3 = 0, \tag{6}$$

where $\hat{\mathbf{o}}$ is the traction vector on the substrate and $\mathbf{u}$ the displacement vector. The components of A_σ and A_u are differential operators and are functions of the elastic constants and density of the coating. We truncate the effective boundary conditions after the linear term in h and use this approximation to derive an analytical expression for the dispersion relation in a coated plate. The plate consists of an isotropic core and two identical anisotropic coating layers. The approximate dispersion relation is obtained from the application of the equations

$$\begin{aligned}
&\partial_m\sigma_{mj} = \rho\partial_t^2 u_j, && -a < x_3 < a,\\
&\sigma_{jm} = \lambda\delta_{jm}\partial_n u_n + \mu(\partial_m u_j + \partial_j u_m),\\
&\hat{\mathbf{o}} \mp h(A_\sigma\hat{\mathbf{o}} + A_u\mathbf{u}) = 0, && x_3 = \pm a,
\end{aligned}$$

with the solution on the form

$$u_j(x_1, x_2, x_3, t) = v_j(x_3)e^{i(kx_1 - \omega t)}.$$

Since the equations of motion above are for an isotropic plate, the solution is straightforward. The result is an analytical expression for the dispersion relation since there is no need to compute quantities associated with the anisotropic coating. To illustrate the behavior of guided waves in the plate, we show exact and approximate dispersion curves for a plate consisting of silver and BSCCO (Bi-2212) layers. The thickness of the silver core is 100 μm and the thickness of each BSCCO coating layer is 5 μm. The material properties of BSCCO are taken from Boekholt *et al.*(1991). Fig. 3a shows the exact dispersion curves for the layered plate and for a plate made of silver only (100 μm thick). The difference between the dispersion curves is significant, except for the lowest modes. A comparison between the approximate dispersion curves and the exact ones for the coated plate is shown in Fig. 3b. We find excellent agreement between the curves except for the highest modes. In Fig. 3c, we show a feature due to the anisotropic coatings. If the propagation direction is not in a plane of elastic symmetry, all waves will couple in the plate (except symmetric and antisymmetric modes). The figure shows a magnification of the exact dispersion curves for the layered plate. The coupling is clearly seen in the figure for the angles $\phi = 45°$ and $\phi = 75°$ since the curves cannot cross. When $\phi = 90°$ the anti-plane waves will decouple from the in-plane ones due to the material symmetry and the curves will cross.

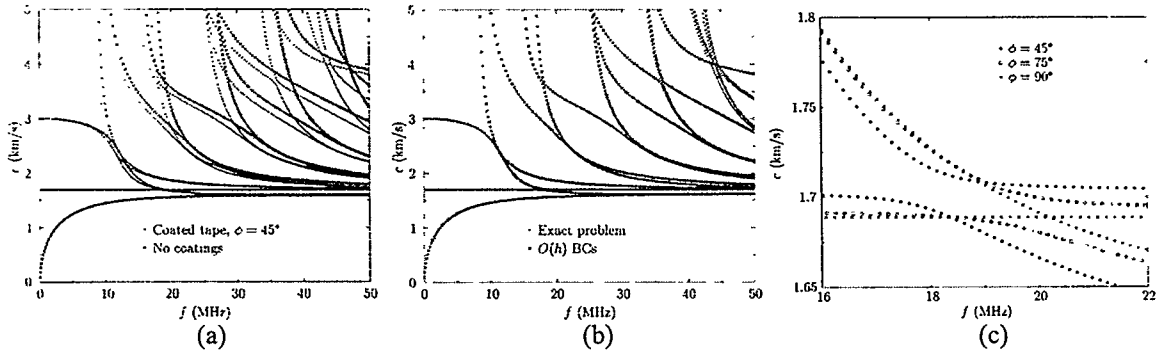

Figure 3 (a) Exact dispersion curves for a coated BSCCO/Ag/BSCCO plate and for an uncoated Ag plate; (b) Exact vs. approximate dispersion curves for the BSCCO/Ag/BSCCO plate; and (c) Magnification of the exact dispersion curves for the BSCCO/Ag/BSCCO plate.

MECHANICAL BEHAVIOR OF BRITTLE/DUCTILE LAYERED SYSTEMS UNDER TRANSVERSE COMPRESSION

We consider a brittle layer, that deforms only elastically, symmetrically sandwiched between two ductile layers that can undergo elastic-plastic deformations. The brittle layer contains a tunnel crack extending form $-a < x_3 < a$ and infinitely extended in the x_1 direction. We consider two types of loading: (i) transverse compression and (ii) axial extension; the latter has been studied extensively (see Hutchinson and Suo, 1991) so here we focus on the former. In the transverse loadcase a load is applied in a frictionless manner perpendicular to the layering. The effects of friction will be considered elsewhere. Here we take both materials to be isotropic and thus the elastic mismatch is characterized by the two well-known Dundurs (1969) parameters α and β. Here we carry out all calculations with $\beta = \alpha/4$. We model the plastic deformation using the Ramberg-Osgood constitutive relation and we compute the energy release rate of the

channel crack using the finite element method. The analysis procedure is similar to that used by Beuth and Klingbeil (1996) to analyze the problem of a cracked film on an infinite substrate; complete calculation details are discussed elsewhere (Sesselmann *et al.*, 1999).

We first discuss the nature of the stress state in the layered structure when subjected to transverse compression. In this case compressive stresses are developed in the x_3 direction, but this is accompanied by lateral expansion (in the x_1 and x_2 directions) due to the Poisson effect. Due to the elastic mismatch between the layered materials, stresses develop in the x_1 and x_2 directions. When the materials deform elastically, the stresses in the brittle layer can be tensile or compressive, depending on the elastic mismatch. When the metal deforms plastically, though, the stresses will be tensile in the brittle layer and thus serve as a driver for transverse cracking. This is significant because the alloys typically used have very low yield strengths; for example, Salib and Vipulanandan (1997) report a yield strength of only 10 MPa for pure Ag used in Ag/BSCCO tapes. In general, the biaxial stress in the brittle layer σ_1 is a function of the elastic mismatch (α, β), the thickness ratio (h_1/h_2), and the plastic properties of the ductile phase (σ_y, n). Figure 4a shows the development of the stresses in the brittle layer as a function of the applied transverse stress for different elastic mismatch (α only as we set $\beta = \alpha/4$) and thickness ratios while Fig. 4b shows the effect of the hardening parameter, n. The results for elastic and elastic-perfect plastic deformations are well-described by an analytical solution that is not discussed here. An important result of these calculations is that the applied transverse stress required to develop a certain tensile stress in the brittle layer increases substantially as the yield stress of the ductile layer increases. Complete results can be found in Sesselmann *et al.* (1999).

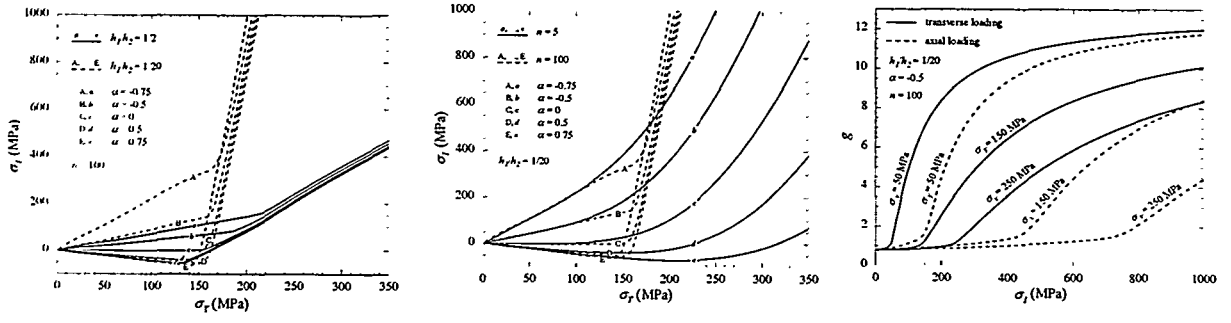

Fig. 4 Influence of elastic mismatch, (a) thickness ratio, and (b) the hardening parameter on the axial stress in the thin layer due to an applied transverse load; (c) comparison of the normalized (by the stress in the brittle layer) energy release rates for transverse and axial loading for different yield stresses of the substrate.

In Fig. 4c we show the normalized energy release rate for tunnel cracking as a function of the applied transverse stress for $h_1/h_2 = 1/20$, $\alpha = -0.5$, and various values of yield properties. The present accuracy in these results after yielding is not certain because we did not model the near-tip behavior in detail, but the qualitative trends are thought to be correct. The energy release rate increases linearly with the applied stress, in accordance with linear elasticity, until yielding occurs at which point, g increases dramatically with increasing σ_T and then reaches an approximate asymptote, the value depending on the elastic mismatch, thickness ratio, and yield properties. The asymptotic g results when the ductile material has fully yielded. For n = 100, the full yielding of the ductile layer occurs rapidly after σ_T reaches σ_y, but development is not as abrupt as n decreases. Of course in the absence of yielding, g never reaches an asymptote as it

increases linearly with σ_T. These results show that increasing σ_y will reduce the susceptibility of the layered material to tunnel cracking.

When the materials undergo only elastic deformations, the energy release rate depends only on the stress in the brittle layer, and not how it is generated as seen by the agreement of the solid and dashed lines in Fig. 4c. This is significant because it allows one to calculate the stress developed when subjected to transverse loading and then simply use the large volume of results that exist in the literature for axial loading to compute the energy release rate. When yielding occurs, though, the results for the axial and transverse load cases depart, and rather significantly. In fact, for a given stress in the brittle layer, the energy release rate for transverse loading exceeds that for axial loading. Thus, while the axial loading results, in terms of the stress in the brittle layer, are not strictly applicable to transverse loading (as they are in the elastic case) once yielding occurs, they can not even serve as conservative estimates. The difference between the axial and transverse loadings is attributed to the fact that once yielding initiates, it develops faster (as the applied load is increased) for transverse loading than for axial loading.

We have extended the analysis for the single crack to the case when multiple cracking occurs in the brittle layer. Under conditions of small-scale yielding the approach is to compute, in the same manner as for the single crack, the energy release rate when the distance between cracks is finite (as opposed to the infinite extent in the previous section). For extensive yielding we resorted to a shear-lag analysis. We computed the normalized energy release rate as a function of crack spacing for various applied stresses for the Ag/ Bi-2212 system and applied these results to measured results in the literature for a Ag/Bi-2212 tape superconductor system (Salib et al., 1997). From their measured stress-strain curve and micrographs of the cracked superconductor (from which we computed the crack density) we used our analysis inversely to infer the fracture toughness of the Bi-2212 superconductor. We find a toughness of 1.2 – 1.8 MPa $m^{1/2}$. This agrees favorably with limited data reported for Bi-2223 (Rouessac and Gomina, 1998).

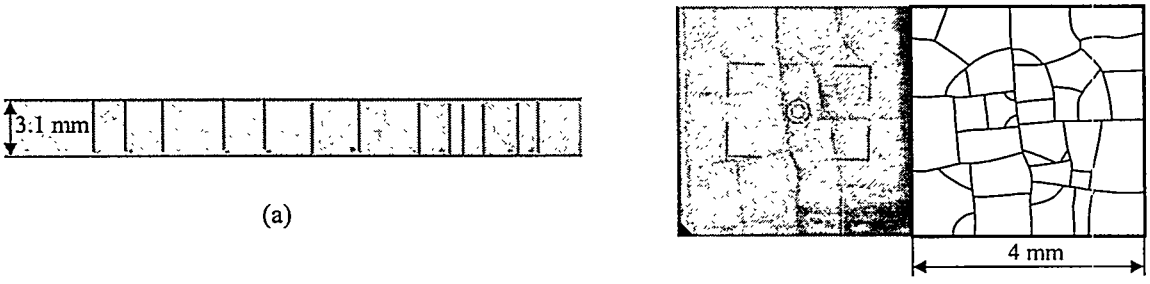

Figure 5 Crack patterns for (a) bending (stress in ceramic at failure = 129 MPa); and (b) transverse loading (applied stress at failure = 40 MPa) in ceramic/epoxy specimens. The lines in (a) are superimposed to highlight crack locations, as is the drawing in (b).

Finally, we are carrying out experiments on model ductile/brittle layered systems in order to both guide and validate our modeling efforts. Specifically we have fabricated epoxy/ceramic layered systems and have performed mechanical tests with axial tension, flexure, and transverse compression loadings. Specimens with the ceramic layer offset from the centerline were used in the flexural experiments to induce tensile stresses in the brittle layer. Representative cracking patterns for the flexural and tensile specimens are similar and are shown in Fig. 5a. For the transverse loading, representative cracking patterns are shown in Fig. 5b. We are in the process

of analyzing these results, carrying out tests under transverse compression biased by axial tension, and making ultrasonic measurements to attempt to quantify the crack density.

ACKNOWLEDGEMENT

This work was performed under the auspices of the U. S. Department of Energy.

REFERENCES

Beuth, J. L. and Klingbeil, N. W., 1996, "Cracking of Thin Films Bonded to Elastic-Plastic Substrates," *J. Mech. Phys. Solids*, 44, pp. 1411-1428.

Beuth, J. L., 1992, "Cracking of Thin Bonded Films in Residual Tension," *Int. J. Solids Structures*, 29, pp. 1657-1675.

Boekholt, M., Harzer, J. V., Hillebrands, B., and Güntherodt, G., 1991, "Determination of the Sound Velocities and the Complete Set of Elastic Constants for $Bi_2Sr_2CaCu_2O_{8+\delta}$ Single Crystal Using Brillouin Light Scattering," *Physica* C, 179, pp. 101-106.

Bövik, P., 1994, "On the Modelling of Thin Interface Layers in Elastic and Acoustic Scattering Problems," Q. *J. Mech. Appl. Math.*, 47, pp. 17-42.

Bövik, P., 1996, "A Comparison Between the Tiersten Model and O(h) Boundary Conditions for Elastic Surface Waves Guided by Thin Layers," *J. Appl. Mech.*, 63, pp. 162-167.

Datta, S. K., Shah, A. H., and Karunasena, W., 1999, "Ultrasonic Waves and Material and Defect Characterization in Composite Plates," to be published in *Mech. Comp. Mat. And Str.*

Ekin, J.W., Finnemore, D. K., Li, Q., Tenbrink, J. and Carter W., 1992, "Effect of axial strain on the critical current of Ag-sheathed Bi-based superconductors in magnetic fields up to 25 T", *Applied Physics Letters*, 61, No. 7, pp. 858-860.

Ekin, J.W., 1998, to be published.

Evans, A.G. and Hutchinson, J.W., 1995, "The thermomechanical integrity of thin films and multilayers", *Acta Metallurgica et Materialia*, 43, No. 7, pp. 2507-2530.

Ho S. and Suo, Z., 1993, "Tunneling Cracks in Constrained Layers," *J. Appl. Mech.*, 60, pp. 890-894.

Hutchinson, J.W. and Suo, Z., 1991, "Mixed mode cracking in layered materials", *Advances in Applied Mechanics*, 29, pp. 63-191.

Karunasena, W. M., Shah, A.H., and Datta, S. K., 1991, "Wave Propagation in a Multilayered Laminated Cross-Ply Composite Plate," *J. Appl. Mech.*, 58, pp. 1028-1032.

Niklasson, A. J., Datta, S. K., and Dunn, M., 1999, "On Approximating Guided Waves in Plates with Thin Ansiotropic Coatings by Means of Effective Boundary Conditions," submitted for publication.

Rouessac and Gomina, 1998, "Anisotropic mechanical properties in sinter-forged bulk highly textured (Bi,Pb)-2223 ceramics," *Journal of the European Ceramic Society*, 18, p. 81-5

Salib, S. and Vipulanandan, C., 1997, "Tensile stress-strain-critical current relationships for silver fiber reinforced BPSCCO composite tapes", *Materials Research Bulletin*, Vol. 32, No. 10, pp. 1333-1340.

Sesselmann, R. Dunn, M. L., and Datta, S. K., to be published.

Shull, P. J., Chimenti, D. E., and Datta, S. K., 1994, "Elastic Guided Waves and the Floquet Concept in Periodically Layered Plates," *J. Acoust. Soc. Am.*, 95, pp. 99-108.

MICROMECHANICS OF MATERIALS WITH CRACKS AND PORES OF DIVERSE SHAPES

Mark Kachanov

Department of Mechanical Engineering, Tufts University,
Medford, Massachusetts 02155,USA

ABSTRACT

Some basic aspects of micromechanics of solids with multiple microcracks and cavities are analyzed. Two groups of properties are addressed:

1. Effective elastic properties. We emphasize *mixtures* of defects of diverse shapes (pores+cracks, etc.) relevant for real materials. Effective elastic moduli of solids with various orientational distributions of cavities are obtained in a unified way. For non-random orientations, the overall anisotropy is found.

2. Likely microfracturing patterns in materials with interacting cavities and cracks and dependence of these patterns on the defect shapes.

INTRODUCTION

The effective properties of solids with cavities strongly depend on the cavity *shapes*. The first problem that arises in this connection is the choice of proper parameters of defect density. We call the density parameters "proper" if the effective properties can be expressed in their terms uniquely and in a unified (with respect to all orientational distributions) way. Such parameters are shape-dependent and their choice is not obvious. For example, porosity - relative volume of pores - becomes inadequate as a density parameter, if pores are non-spherical. The choice of proper density parameters is actually dictated by the structure of the elastic potential.

Our analysis utilizes recent results of [3] briefly reviewed below.

We start with the general relation for a representative volume element V of a linear elastic solid containing N traction free defects (cracks or cavities) with surfaces F^{ν}. The conventional starting point for the analysis is the representation of the macroscopic strain ε associated with V under the applied macroscopic stress σ in the form

$$\sigma = S^0 : \varepsilon + \Delta\varepsilon \qquad (1)$$

The first term is the strain due to deformation of the matrix (S^0 is the compliance tensor of the matrix material) and the second term is due to defects. Finding the effective compliances S_{ijkl} (such that $\varepsilon = S : \sigma$) is thus reduced to finding $\Delta\varepsilon$ in terms of σ.

As follows from the divergence theorem, the extra strain $\Delta\varepsilon$ due to one cavity is given by the integral over the cavity boundary F:

$$\Delta\varepsilon = \frac{1}{2V}\int_F (\boldsymbol{un} + \boldsymbol{nu})dF \qquad (2)$$

where $\boldsymbol{u}$ is the displacement vector and $\boldsymbol{n}$ is the unit normal to F. In the 2-D case, volume V changes to a representative area A and cavity surfaces - to hole lines.

In the important case of a *crack*, this term reduces to

$$\Delta\varepsilon = \frac{1}{2V}\int_F ([\boldsymbol{u}]\boldsymbol{n} + \boldsymbol{n}[\boldsymbol{u}])dF \qquad (2a)$$

where $[\boldsymbol{u}] = \boldsymbol{u}^+ - \boldsymbol{u}^-$ is the displacement discontinuity vector across the crack surface F. In the case of a *flat* crack ($\boldsymbol{n}$ is constant along F)

$$\Delta\varepsilon = \frac{1}{2V}(\boldsymbol{bn} + \boldsymbol{nb})F \qquad (2b)$$

where $\boldsymbol{b} = \langle[\boldsymbol{u}]\rangle$ is the average over F displacement discontinuity vector.

Due to linear elasticity of the solid, $\Delta\varepsilon$ is a linear function of the applied stress σ:

$$\Delta\varepsilon = \boldsymbol{H} : \sigma \text{ or, in components } \Delta\varepsilon_{ij} = H_{ijkl}\sigma_{kl} \qquad (3)$$

where the fourth rank tensor $\boldsymbol{H}$ (possessing the usual symmetries $H_{ijkl} = H_{jikl} = H_{ijlk} = H_{klij}$) is the *cavity compliance tensor*. Finding $\boldsymbol{H}$ requires calculation of the integral (2) in terms of the applied stress. This has been done for a number of *2-D* hole shapes (elliptical, polygonal, rectangular and hypotrohoidal) and for *3-D* ellipsoids [1-3]

In the case of *many* cavities, we shall first consider the approximation of non-interacting defects: each cavity is placed into the externally applied stress σ (does not experience any influence of neighbours) and $\Delta\varepsilon$ -contributions of individual cavities are summed up. This approximation is important because (A) it is rigorous at small defect densities and (B) it constitutes the basic building block for most of the existing approximate schemes (that place non-interacting defects into some sort of "effective" environment).

We illustrate the basic ideas of our analysis on the example of 2-D *elliptical holes.*

NONINTERACTING ELLIPTICAL HOLES

For an elliptical hole having axes $2a$, $2b$ with unit normals $\boldsymbol{n}$, $\boldsymbol{m}$, correspondingly,

$$\boldsymbol{H} = \frac{\pi}{AE_0}\left[a(2a+b)\boldsymbol{nnnn} + b(2b+a)\boldsymbol{mmmm} + \frac{1}{2}(a+b)^2(\boldsymbol{mn}+\boldsymbol{nm})(\boldsymbol{mn}+\boldsymbol{nm}) - ab(\boldsymbol{mmnn}+\boldsymbol{nnmm})\right] \tag{4}$$

The first two terms characterize the normal compliances of the hole in the $\boldsymbol{n}$, $\boldsymbol{m}$ - directions, the third term - the shear compliance and the fourth term - the Possson's ratio effect.

The elastic potential in terms of stresses (complementary energy density) of a solid with a cavity can be represented as a sum of two terms:

$$f(\sigma) = (1/2)\sigma : \varepsilon(\sigma) = (1/2)\sigma : S^0 : \sigma + (1/2)\sigma : \boldsymbol{H} : \sigma \equiv f_0 + \Delta f \tag{5}$$

where f_0 is the potential in the absence of the cavity (in the case of the isotropic *2-D* matrix, $f_0 = (1/2E_0')\left[(1+\nu_0')tr\sigma\cdot\sigma - \nu_0'(tr\sigma)^2\right]$ where E_0', ν_0' are Young's modulus and Poisson's ratio E_0', ν_0' for plane strain and $E_0/(1-\nu_0'^2)\ \nu_0'/(1-\nu_0')$ for plane stress) and Δf is due to the cavity. With (4), Δf assumes the form that reflects the hole geometry:

$$\Delta f = \frac{1}{2E_0 A}\left\{\pi ab\left[4tr(\sigma\cdot\sigma) - (tr\sigma)^2\right] + 2\pi\sigma\cdot\sigma : \left(a^2\boldsymbol{nn} + b^2\boldsymbol{mm} - ab\boldsymbol{I}\right)\right\} \tag{6}$$

The first term in the braces is expressed in terms of stress invariants, and thus describes the isotropic response; it enters with the ellipse's area πab as a multiplier. It vanishes in the case of a *crack*. The second term is orientation-dependent; it vanishes for a *circular* hole.

For *many nonineracting* holes, each hole is placed into the externally applied stress σ. The strain due to holes $\Delta\varepsilon = \sum \boldsymbol{H}^{(k)} : \sigma$, so that Δf is a sum of terms of the (6)-type:

$$\Delta f = \sigma : \sum \boldsymbol{H}^{(k)} : \sigma = \frac{1}{2E_0}\left\{p\left[4tr(\sigma\cdot\sigma) - (tr\sigma)^2\right] + 2\sigma\cdot\sigma : (\beta - p\boldsymbol{I})\right\} \tag{7}$$

Thus, the potential is expressed in terms of *two hole density parameters*:

scalar (porosity) $$p = \frac{\pi}{A}\sum (ab)^{(k)} \tag{8}$$

2nd rank hole density tensor $$\beta = \frac{\pi}{A}\sum \left(a^2\boldsymbol{nn} + b^2\boldsymbol{mm}\right)^{(k)}$$

We emphasize that the density parameters - porosity p and tensor β - are not introduced arbitrarily, but are *dictated by the structure of the elastic potential.* Note that all elliptical shapes (eccentricities b/a) are covered in a unified way and no degeneracies arise for cracks. *Mixtures* of diverse holes (for example, circles+cracks) are also covered.

The representation (7) yields interesting (and not intuitively obvious) conclusions. Since the elastic anisotropy is determined by the 2-nd rank tensor ϕ which is symmetric (as a sum of symmetric tensors), a solid with *any* orientational distribution of ellipses is *orthotropic*. Moreover, the orthotropy is of a simplified type: (A) Young's modulus variation with direction is described by an ellipse, rather than by a 4-th order curve, and (B) the number of independent constants is reduced from four, as in the general case of 2-D orthotropy, to three (the shear modulus is expressed in terms of Young's moduli and Poisson's ratios, see 10_3).

Effective elastic moduli S_{ijkl} for any orientational distribution of ellipses follow from the potential (since $\partial f/\partial\sigma_{ij}=\varepsilon_{ij}=S_{ijkl}\sigma_{kl}$). In the principal axes x_1x_2 of β, the effective Young's moduli, Poisson's ratios and the shear modulus are

$$E_{\{1,2\}}=\frac{E_0}{1+p+2\{\beta_{11},\beta_{22}\}};\quad \frac{1}{G_{12}}=\frac{1+\nu_{12}}{E_1}+\frac{1+\nu_{21}}{E_2}$$
$$\{\nu_{12},\nu_{21}\}=\frac{\nu_0+p}{1+p+2\{\beta_{11},\beta_{22}\}} \qquad (10)$$

Even in the simplest case of randomly oriented holes (isotropy), porosity alone is not a sufficient density parameter. Indeed, in this case the effective Young's and bulk moduli are

$$E=\frac{E_0}{1+3p+q};K=\frac{K_0}{1+(2p+q)/(1-\nu_0)} \qquad (11)$$

where an (additional to porosity p) "eccentricity" parameter emerges:

$$q=tr\beta-2p=(\pi/A)\sum(a-b)^{(k)2} \qquad (12)$$

If this shape factor is ignored (holes are treated as circular), then porosity, as inferred from the data on the effective moduli, may be substantially overestimated. For example, porosity estimated from the bulk modulus K/K_0 would be exaggerated by a factor of $1+q/2p$.

SOLIDS WITH INTERACTING HOLES

Interacting holes are usually considered in the framework of approximate schemes. A number of such schemes has been proposed. Their predictions differ from each other, with the magnitude of the differences dependent upon the cavity shapes [3].

Discussions of adequacy of these schemes is meaningful only if the statistics of mutual positions of defects is specified. We restrict the discussion to the case of *random* mutual positions (otherwise, the effective properties will depend on the particular spatial pattern, as illustrated by the periodic arrays, where the results depend on the lattice parameters).

The existing approximate schemes can be classified, roughly, into two groups (with the exception of the virial construction techniques, where several calculations of the term quadratic in defect density have been made):

(A) Effective matrix schemes (self-consistent, generalized self-consistent, differential);

(B) Effective field schemes (in particular, Mori-Tanaka's scheme, MTS).

Both A- and B-methods reduce the analysis to non-interacting defects that are placed into some sort of effective environment: effective matrix (in the A-methods) or effective stress field (in the B-methods). The B-methods appear to be more phusically sound, particularly in the context of stress superpositions. Indeed, representing the problem with N interacting defects as a superposition of N problems with one defect each, we describe the interaction effects by the additional, interaction tractions induced at the site of k-th cavity by (in the k-th subproblem) by the other cavities in the remaining sub-problems. In MTS, these additional tractions are taken as induced by the average over the solid phase stress σ^s. This seems reasonable in the case of random mutual positions of defects.

For a solid with traction free cavities, the average over the solid phase σ^s is found in terms of the applied (macroscopic) stress σ and porosity by using the divergence theorem:

$$\sigma_{ij}^s = \frac{\sigma_{ij}}{1-p} \tag{13}$$

Thus, placing a representative hole into σ^s yields the potential $\Delta f = (1/2)\sigma : \Delta\varepsilon$ in MTS approximation, by replacing $\sigma \to (1-p)^{-1}\sigma$ in the hole compliance relation $\Delta\varepsilon = \boldsymbol{H} : \sigma$ as follows:

$$\Delta f = \frac{1}{1-p}\Delta f_{non\,int} = \frac{1}{1-p}\frac{1}{2E_0}\left\{p\left[4tr\sigma\cdot\sigma - (tr\sigma)^2\right] + 2\sigma\cdot\sigma : (\beta - p\boldsymbol{I})\right\} \tag{14}$$

For *cracks*, $p = 0$ and MTS coincides with the non-interaction approximation, implying that the competing interaction effects of stress shielding and amplification, on average, balance each other. This is related to the fact that the presence of cracks does not change the average stress in the matrix (provided the boundary conditions are in tractions): $\sigma^s = \sigma$.

In the case of *randomly oriented* elliptical holes, the effective moduli are

$$E = \frac{E_0}{1 + (3p+q)(1-p)^{-1}};\quad K = \frac{K_0}{1 + (1-p)^{-1}(2p+q)/(1-\nu_0)} \tag{15}$$

where the factor $(1-p)^{-1}$ accounts for interactions.

We consider now a *mixture of interacting circular holes and cracks*. In this case, $\beta = \beta_{holes} + \beta_{cracks} = p\boldsymbol{I} + p\alpha$ where α is the crack density tensor and

$$\Delta f = \frac{1}{1-p}\Delta f_{non\,int} = \frac{1}{2E_0}\left\{\frac{p}{1-p}\left[4tr\sigma\cdot\sigma - (tr\sigma)^2\right] + \frac{2p}{1-p}\sigma\cdot\sigma : \alpha\right\} \tag{16}$$

The first term in the braces depends on p and is independent of the crack density tensor α; the second term contains *both* α and p. This shows that, since cracks do not raise the average stress in the solid, as far as the effective properties are concerned, they produce no impact on holes, whereas *holes enhance the impact of cracks on the effective moduli* (by changing the average stress environment for cracks). Thus, in the problem of effective properties, *cracks do not affect holes, but holes affect cracks.*

If cracks in such a mixture are *randomly oriented*, $\alpha=(\rho/2)\boldsymbol{I}$ where $\rho=tr\alpha=\sum a^{(k)2}$ is the usual scalar crack density, so that $\beta=p(1+\rho/2)\boldsymbol{I}$ and

$$E=\frac{E_0}{1+(3p+\pi\rho)(1-p)^{-1}} \quad K=\frac{K_0}{1+(1-p)^{-1}(2p+\pi\rho)/(1-\nu_0)} \tag{17}$$

For the mixture of *parallel cracks* (normal to the x_1 axis) and circles, $\alpha=\rho e_1 e_1$. Young's modulus in the direction normal to cracks and the ratio E_1/E_2 (the degree of anisotropy)

$$E_1=\frac{E_0}{1+(3p+2\pi\rho)(1-p)^{-1}}; \quad \frac{E_1}{E_2}=\frac{1+3p(1-p)^{-1}}{1+(3p+2\pi\rho)(1-p)^{-1}} \tag{18}$$

An interesting issue for the mixtures cracks+pores is whether the anisotropy due to preferential crack orientations is enhanced of weakened by the "background" porosity p. The anisotropy is affected by p through two competing mechanisms: (A) in the absence of interactions, porosity reduces the anisotropy; (B) interactions between pores and cracks enhance the impact of cracks; in particular, they enhance the anisotropy. The result (18) shows that $\partial(E_1/E_2)/\partial p>0$, i.e., the first mechanism is dominant: *porosity weakens the crack-induced anisotropy*.

LARGE HOLE-SMALL HOLE INTERACTION

When fracture of porous materials is considered, an important question is whether the highest tensile hoop stress occurs at a smaller hole ("microhole") or at a larger one. The answer depends on the shapes of holes. In particular, in the two limiting cases - circular holes and cracks - the answers are opposite. Indeed, for a *single circular* hole, the maximum hoop stress under remote tension p is $3p$: the concentration factor of 3 is independent of the hole size. Consider now the system "large circular hole - small circular hole". Since the impact of a larger hole on a smaller one is stronger than vice versa, the highest concentration factor is expected at the boundary of the smaller hole. This implies that, as the critical load is reached, it is the smaller hole that will fracture and "advance" towards the larger one.

In the system "large *crack* - small *crack*", collinear arrangement, the opposite is true: $K_I(B)>K_I(A)$. This implies that, at the critical load, fracture starts at the *larger* crack. This result is explained by the fact that, for an *isolated* crack of length $2l$ under remote tension p, $K_I=p\sqrt{\pi l}$ i.e. is higher for a larger crack; this factor is dominant, as compared to the impact of interaction.

These two extreme cases indicate that, for interacting *elliptical* holes, the pattern is not obvious and will depend on eccentricities of the holes and spacings between them.

If both holes have the *same* eccentricity $\lambda=b/a\le 1$, the highest hoop stress will occur at the *smaller* hole boundary. Indeed, the stress concentration factor for a single isolated hole $1+2/\lambda$ is the same at both holes. Due to a stronger "amplifying" impact of a larger hole on the smaller one than vice versa, it is the smaller hole where the highest hoop stress occurs. A similar

conclusion will, obviously, hold for the system "larger hole with larger λ - smaller hole with smaller λ".

A less obvious and more interesting case is the configuration "larger hole with smaller λ - smaller hole with larger λ". The point of the highest hoop stress is then determined by the competition of two mechanisms: (A) in the absence of interaction, the hole with smaller eccentricity has a higher stress concentration and (B) larger hole produces a stronger impact on the smaller one than vice versa. We investigated this case numerically using the "stress feedback" procedure (alternating technique) [4].

Fig. 1 shows the eccentricity λ of a larger hole interacting with a small *circular* hole for which the situation is "neutral": the stress concentration is the same at both holes. (The major axis a of the larger hole remains equal to 3 diameters of the smaller hole while its minor axis b is varied.) Points lying below (above) the curve correspond to the highest hoop stress occurring at the boundary of the larger (smaller) hole. At larger distances, the interaction weakens and even a slight ellipticity of the larger hole (λ close to 1) results in shifting of the point of the highest stress from the smaller to the larger hole.

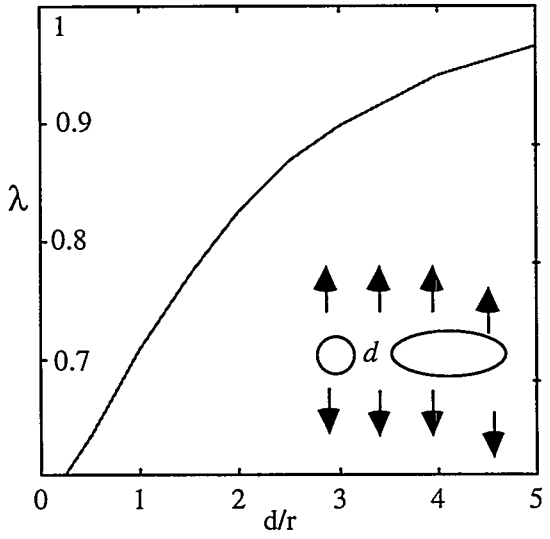

Fig. 1: Parameters required for a "neutral" configuration.

MICROFRACTURING PATTERNS

Consider now the interaction of a larger hole with a number of smaller ones. This configuration may be relevant for a porous medium microstructure. In the first approximation, the interaction between small holes can be ignored, as compared to the "large hole - small hole" interactions. Then, the results obtained above can be utilized. Assuming that fracturing starts at the point of the highest tensile hoop stress, Fig. 2 shows the likely microfracturing patterns.

For a *crack* interacting with micropores, fracture initiates at the crack tip (Fig. 2a).

If the shape of the larger hole is close to *circular*, the micropores (and microcracks) will advance towards the larger hole, independently of their shapes (Fig. 2b).

For a *strongly elongated hole* (small λ) interacting with more or less circular microholes, the pattern of fracture initiation will depend on the spacing between the holes. If the distances between the large hole and the microholes are small, then the smaller holes will fracture first and, presumably, will crack towards larger hole (Fig. 2c). At larger distances (solid with smaller density of micropores), the pattern shifts to the opposite one: the interaction effect is weak and fracture initiates at the larger holes (Fig. 2d).

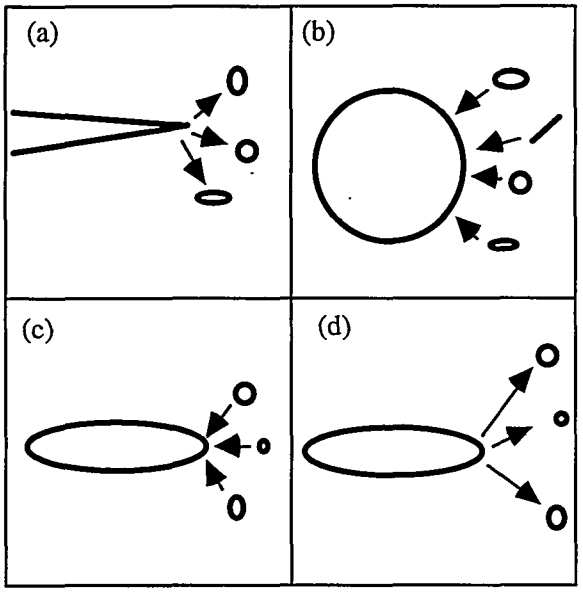

Fig. 2: Likely microfracturing patterns.

ACKNOWLEDGMENTS

This research was supported by the DOE and NSF through grants to Tufts University.

REFERENCES

1. M. KACHANOV. Elastic solids with many cracks and related problems. In: *Advances in Applied Mechanics* (J.W. Hutchinson & T.Y. Wu Eds.), 259-445, Academic Press (1993).

2. I. TSUKROV and M. KACHANOV., Solids with holes of irregular shapes: effective moduli and anisotropy. *International Journal of Fracture*, **64**, R9-R12 (1993).

3. M. KACHANOV, I. TSUKROV and B. SHAFIRO, Effective moduli of solids with cavities of various shapes, *Applied Mechanics Reviews*, **47**, S151-S174 (1994).

4. I. TSUKROV. and M. KACHANOV, Stress-concentrations and microfracturing patterns for interacting elliptical holes, *International Journal of Fracture*, **89**, R89-R92 (1994).

AN INVESTIGATION OF DYNAMIC CRACK INITIATION IN DUCTILE STEELS USING HIGH SPEED INFRARED THERMOGRAPHY

A.J. Rosakis, G. Ravichandran and P.R. Guduru

Graduate Aeronautical Laboratories
California Institute of Technology
Pasadena, CA 91125

ABSTRACT

The goal of the work presented here is to study dynamic crack initiation in ductile steels (Ni-Cr steel and 304 stainless steel) at different loading rates and to establish appropriate dynamic failure criteria. A variety of infrared and visible optical methods and high-speed photography are used in this study. Precracked steel specimens are subjected to dynamic three-point bend loading by impacting them in a drop weight tower. During the dynamic deformation and fracture initiation process the time history of the transient temperature in the vicinity of the crack tip is recorded experimentally using a high-speed infrared detector. The dynamic temperature trace in conjunction with the HRR solution is used to determine the time history of the dynamic J-integral, $J^d(t)$, and to establish the dynamic fracture initiation toughness, J^d_c. The measurements made using high-speed thermography are validated through comparison with determination of $J^d(t)$ by dynamic optical measurements of the crack tip opening displacement (CTOD).

1. INTRODUCTION

To aid in the design and vulnerability analysis of impact loaded structures and energy systems (e.g., pressure vessels, pipelines and reactors), it is necessary to quantify the mechanical behavior and failure modes of materials used in such systems under carefully controlled conditions. Because of design constraints and safety issues, these energy systems are typically

fabricated with corrosion resistant and highly ductile metallic alloys such as stainless and Ni-Cr steels. Yet, relatively little is known regarding dynamic crack initiation and growth in such ductile metals. A major stumbling block in this area is the measurement of relevant fracture parameters, such as the *J*-integral, under a combination of large scale yielding conditions and dynamic loading. Considerable effort has been made towards the analytical and computational characterization of fracture parameters in highly ductile metals [1-4]. Recently, several researchers have presented detailed analyses of ductile fracture using higher order expansions of the deformation fields within the plastic zone [5-7].

To date relatively little experimental work has been done on determining fracture parameters, such as $J^d(t)$, for ductile fracture under dynamic loading conditions. The only direct measurements of the dynamic value of the *J*-integral, $J^d(t)$, have been made using the optical technique of caustics in conjunction with high-speed photography [8]. However, even this approach employs a procedure using calibration of *J* versus the caustic diameter, *D*, under quasi-static loading conditions and then extends the same to dynamic loading conditions. Hence, this technique is limited to rate-insensitive materials and requires calibration for all combinations of specimen material and specimen geometry.

The current study introduces a technique for measurement of temperature variation in the vicinity of the dynamically loaded crack tip using a high speed infrared detector to determine the time history of the dynamic value of the J-integral, $J^d(t)$. The dynamic temperature trace is also employed to establish the dynamic fracture initiation toughness, $J^d(t_c) = J^d_t$, where t_c is the time of fracture initiation. The measurements made using high-speed thermography are validated through comparison with determination of $J^d(t)$ by dynamic optical measurements of the crack tip opening displacement (CTOD).

2. EXPERIMENTAL SETUP

In this investigation high-speed infrared measurements of temperature and optical measurements of crack tip opening displacements were employed to study dynamic crack initiation in precracked ductile steel specimens. In the former, the temperature increase ahead of the crack tip during dynamic deformation is measured and is related to the dynamic *J* integral. In the latter, the dynamic *J* integral is estimated by relating it to the measured crack opening displacement history.

2.1 Specimen Configuration, Loading Arrangement and Material Properties

The experiments employed edge cracked specimens in a three point bend configuration. The specimens were fabricated out of 2.3 Ni- 1.3 Cr steel (will be referred to as Ni-Cr steel here onwards, 0.17C, 0.3Mn, 0.13Cu, 0.22Si, 0.25Mo) and 304 stainless steel (0.024C, 1.77Mn, 0.28Cu, 0.33Si, 8.16Ni, 18.33Cr, 0.35Mo, 0.1Co). The relevant material properties for these two steels are listed in Table 1. Ni-Cr steel is strain-rate sensitive, with about 15% increase in yield stress at a strain rate of 1000/s compared to that at 0.001/s. On the other hand, 304 stainless steel is relatively rate insensitive and does not exhibit any appreciable change in yield properties for the same change in strain rate. Dimensions for the edge-cracked specimen are shown in Figure 1. An initial crack length of 30 mm was machined using electric discharge machining (EDM) that resulted in a notch 0.25 mm wide. The test specimens were dynamically loaded in a 3-point bend

configuration by subjecting them to impact in a Dynatup 8100A drop weight tower. A tup mass of 200kg and an impact velocity of 5 m/s were employed for all the experiments conducted. The dynamic deformation and fracture initiation process were monitored using high-speed infrared measurement of temperature and optical measurement of crack tip opening displacements. Details of the two experimental techniques are presented in the following sections.

2.2 Infrared Temperature Measurements

In this first series of experiments high-speed infrared diagnostics were introduced to study dynamic crack initiation for the first time in precracked ductile steel specimens impact loaded in a three point bend configuration. As the specimen was loaded, a high speed HgCdTe infrared detector was employed to record the evolution of the temperature trace at a pre-determined location from the crack tip, as shown in Figure 2. A Newtonian optical arrangement

Table 1

Material properties for Ni-Cr steel and 304 stainless steel

Properties	Ni-Cr	304 Stainless
Young's Modulus, E (GPa)	205	193
Density, ρ (kg/m^3)	7910	7900
Specific Heat, c_p (J/Kg-K)	460	500
Yield Stress, σ_0 (MPa) ($\dot{\varepsilon} = 10^{-3} s^{-1}$)	750	510
Hardening Exponent, n ($\dot{\varepsilon} = 10^{-3} s^{-1}$)	8	7

is employed to collect the radiation and focus it onto the detector. The location of the area of interest on the specimen, which is essentially the area of temperature measurement, is situated well within the plastic zone that engulfs the dynamically loaded crack tip, as shown in Figure 2(b). If this temperature measurement is made at an appropriate location within the fracture process zone surrounding the dynamically loaded crack tip then, as it will be shown later, the history of the temperature trace can be directly related to the evolution of the dynamic

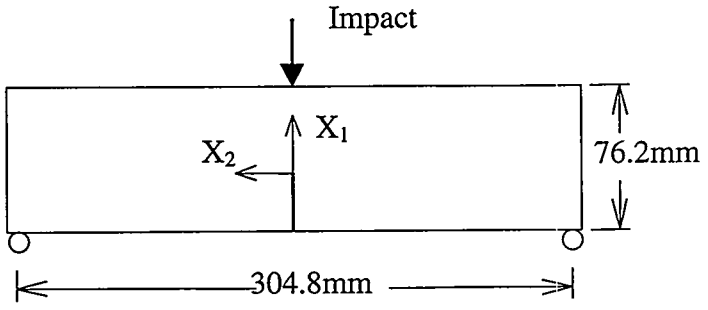

Thickness = 10 mm

Precrack Length = 30 mm Notch Width = 0.25mm

Figure 1. Schematic of three-point bend impact Loading of a precracked steel specimen

value of the J-integral, $J^d(t)$.

2.3 Optical Measurements of the Crack Tip Opening Displacement (CTOD)

In order to corroborate and evaluate the accuracy and applicability of the infrared temperature measurement technique to determine $J^d(t)$, optical measurements of the crack tip opening displacement (CTOD) were performed to measure the time history of the dynamic value of the J-integral, $J^d(t)$. The optical arrangement for the CTOD measurement employs a cavity dumped pulsed laser as the illumination source and a high-speed camera as the imaging system. A collimated laser beam is incident on the steel specimen, passes through the crack opening and is imaged on to the film track of a rotating mirror type high-speed camera (2 million frames/second). A schematic arrangement of the setup is shown in figure 3. The crack tip opening displacement is later measured directly from the recorded crack opening profiles.

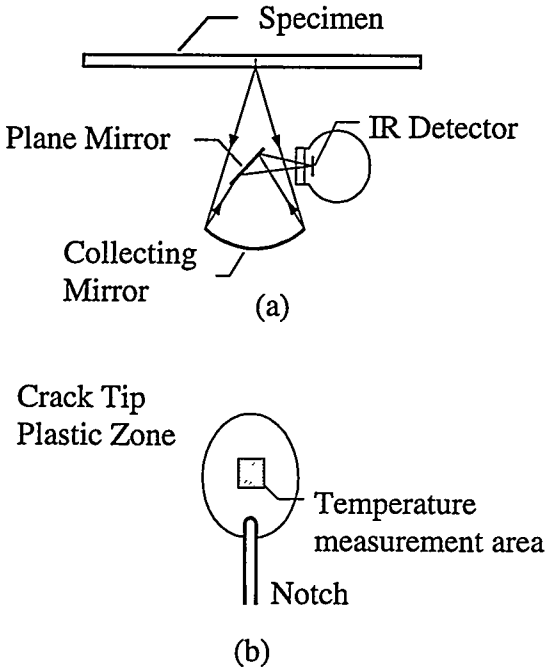

Figure 2. Measurement of temperature variation in the vicinity of the dynamically loaded crack tip, (a) top view of specimen and (b) location of temperature measurement area

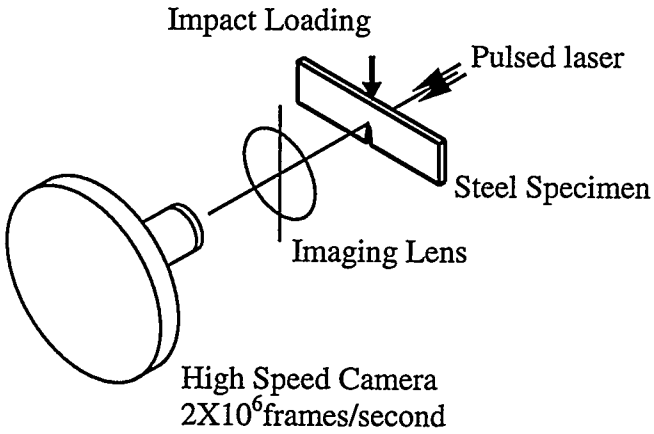

Figure 3. Optical measurement of crack tip opening displacement (CTOD) using high-speed photography.

3. ANALYSIS PROCEDURE

The temperature measurements made in the vicinity of the dynamically loaded crack tip and the optical measurements of the crack tip opening displacement were analyzed to determine the time history of the dynamic value of the J-integral, $J^d(t)$. The analysis procedure involves the application of an appropriate asymptotic field that describes the crack tip stresses in an elastic-plastic material. The details of the analysis procedure are discussed in the following sections.

3.1 Temperature Rise Associated with the HRR Singular Field

Hutchinson[1] and Rice and Rosengren [2], collectively referred

to as HRR, considered the case of a monotonically loaded stationary crack in a material described by a J_2-deformation theory of plasticity and a power hardening relationship and showed that the strain components in the crack tip region scale with the value of the *J*-integral. This enables one to relate the J integral to temperature rise ahead of the crack tip.Consider an elastic-plastic isotropic homogeneous material with constant thermal conductivity. The heat conduction equation can be written as

$$k\nabla^2\Theta - \alpha(3\lambda + 2\mu)\Theta_0\dot{\varepsilon}^e_{kk} + \beta\sigma_{ij}\dot{\varepsilon}^p_{ij} = \rho c\dot{\Theta} \qquad (1)$$

where, k is the thermal conductivity, Θ is the absolute temperature, α is the coefficient of thermal expansion, λ and μ are Lame elastic constants, Θ_0 is the initial temperature, ε_{ij} and σ_{ij} are the Cartesian components of the strain and stress tensors, ρ is the mass density, and c is the specific heat. The quantity β is the fraction of plastic work rate density, $\dot{W}^p = \sigma_{ij}\dot{\varepsilon}^p_{ij}$, dissipated as heat. Neglecting the thermo-elastic term and assuming adiabatic conditions, equation (1) becomes

$$\frac{\beta}{\rho c}\sigma_{ij}\dot{\varepsilon}^p_{ij} = \dot{\Theta} \qquad (2)$$

Substituting HRR field equations into equation (2) we have

$$\dot{J}^d(t) = \frac{\rho c I_n}{\beta}\left(\frac{n+1}{n}\right)\frac{r}{\Sigma_{ij}(\theta,n)E_{ij}(\theta,n)}\dot{\Theta}(r,\theta,t) \qquad (3)$$

On integrating equation (3) with respect to time, t, we obtain

$$J^d(t) = \frac{\rho c I_n}{\beta}\left(\frac{n+1}{n}\right)\frac{r}{\Sigma_{ij}(\theta,n)E_{ij}(\theta,n)}[\Theta(r,\theta,t) - \Theta_0(r,\theta,t_0)] + J^d_0(t_0) \qquad (4)$$

where $J^d_0(t_0)$ is the value of the *J*-integral at time $t = t_0$ and represents the integration constant. Equation (6) relates the time history of the dynamic value of the *J*-integral, $J^d(t)$, to the dynamic temperature rise in the vicinity of the crack tip.

3.2 Crack Tip Opening Displacement (CTOD) Associated with the HRR Singular Field

Using the 90^0 intercept definition for CTOD as used by Shih [9], the J integral can be related to CTOD as

$$J = \frac{\sigma_0}{d_n(\varepsilon_0, n)}\delta \qquad (5)$$

where, δ is the CTOD, J is the value of the *J*-integral, σ_0 is the yield stress and d_n is a material dependent dimensionless constant.

4. EXPERIMENTAL OBSERVATIONS AND RESULTS

Typical variations of temperature measured in the vicinity of the crack tip for a dynamically loaded Ni-Cr steel specimen are shown in Figure 4. Traces from two nominally similar experiments are plotted. There are a few features in the temperature traces that merit elucidation. At about 550 μs after impact the temperature detection area is completely engulfed by the crack tip plastic zone and the transient temperature signal starts to increase steadily in a

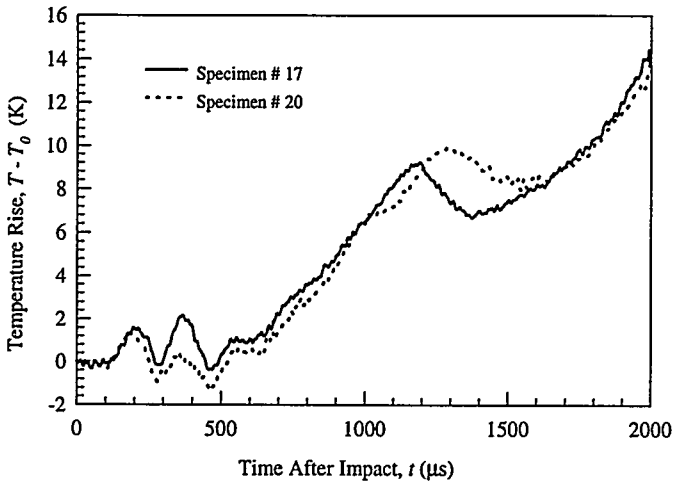

Figure 4. Time history of the temperature variation in the vicinity of the dynamically loaded crack tip for a precracked Ni-Cr steel specimen.

monotonic fashion. This increase remains steady until about 1200-1300 μs when a dip occurs in the temperature trace, which corresponds to fracture initiation.

The transient temperature traces were analyzed using equation (4) to determine the evolution of the instantaneous value of the J-integral, $J^d(t)$. Figure 6 shows typical results from two experiments.

Infrared thermography was also employed to study ductile failure of edge-cracked 304 stainless steel specimens subjected to three-point bend impact loading. Figure (5) shows typical variations of temperature measured in the vicinity of the dynamically loaded crack tip for a 304 stainless steel specimen. Traces from two nominally similar experiments are plotted. Features similar to those observed for Ni-Cr steel can be observed in this case also.

As discussed earlier, optical measurements of the crack tip opening displacements were made using a high-speed imaging system in order to validate the infrared thermography measurements of $J^d(t)$. The dynamic value of the CTOD, $\delta^d(t)$, was using the 90° vertex intercept definition. Thereafter, time history of the dynamic value of the J-integral, $J^d(t)$, was determined from the CTOD variation in accordance with equation (5). Figure 6 shows the time history of the dynamic J-integral, $J^d(t)$, as determined from measurements of the dynamic CTOD, $\delta^d(t)$. The figure also shows the variation of $J^d(t)$ as determined from infrared measurements of temperature. The excellent degree of correspondence between the two establishes the validity and accuracy of the infrared thermography technique to determine $J^d(t)$.

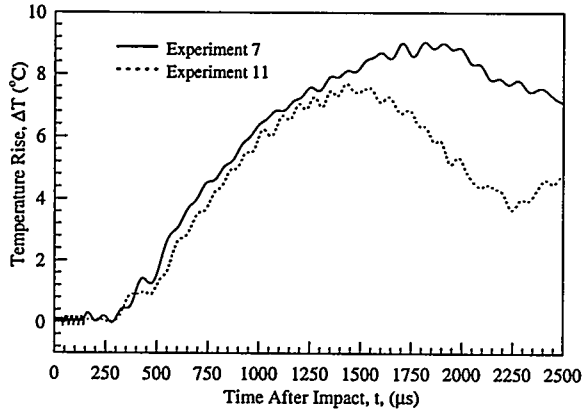

Figure 5. Time history of the dynamic temperature variation in the vicinity of the dynamically loaded crack tip for a pre-cracked 304 stainless steel specimen.

Table 2 lists the values of fracture initiation toughness, $J(t_c) = J_c$, obtained for quasi-static loading conditions and for dynamic loading. Fracture toughness values for both the steels are listed. The rate of loading at the time of fracture, $t = t_c$, is quantified in terms of the value of the rate of change of the J-integral. As can be seen from this data there is a significant increase in the value of the fracture toughness with increasing rate of loading for Ni-Cr steel. No such significant rise is observed for the 304 stainless steel.

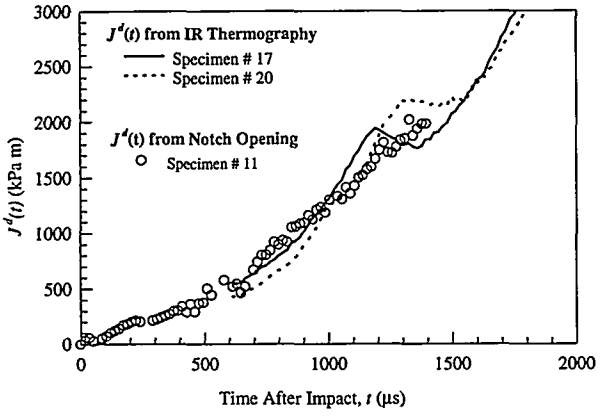

Figure 6. Time history of the dynamic value of the J-integral as obtained from optical measurement of CTOD and infrared temperature measurement (Ni-Cr steel)

Table 2

Fracture toughness as a function of loading rate for Ni-Cr steel and 304 stainless steel

Ni-Cr Steel		304 Stainless Steel	
$\dot{J}^d_{crit}$	J^d_{crit}	$\dot{J}^d_{crit}$	J^d_{crit}
10 $kNm^{-1}s^{-1}$	1080 kNm^{-1}	8 $kNm^{-1}s^{-1}$	1800 kNm^{-1}
2500 $kNm^{-1}s^{-1}$	1750 kNm^{-1}	1300 $kNm^{-1}s^{-1}$	1600 kNm^{-1}

5. SUMMARY

This study focuses on the development of a non-contact experimental technique to measure the history of the J integral for dynamically loaded cracks in ductile solids. This technique utilizes infrared thermography for the first time to measure the temperature increase ahead of the dynamically deforming crack, which is subsequently related to the J integral through HRR singular fields. The accuracy of this method is verified through an independent measurement of the dynamic J integral, where high-speed photography was used to measure the crack tip opening displacement (CTOD).

ACKNOWLEDGEMENTS

The authors would like acknowledge the support of the Department of Energy under grant no. DE-FG03-95 ER14560 (Dr R.E. Price, Program Manager).

REFERENCES

1. Hutchinson, J. W., Singular Behavior at the End of a Tensile Crack in a Hardening Material, *Journal of Mechanics and Physics of Solids*, 16, 13 (1968).

2. Rice, J. R., and Rosengren, G. F., Plane Strain Deformation Near a Crack Tip in a Power-Law-Hardening Material, *Journal of the Mechanics and Physics of Solids*, 16, 1 (1968).

3. Needleman, A., and Tvergaard, V., An Analysis of Ductile Rupture Modes at a Crack Tip, *Journal of the Mechanics and Physics of Solids*, 35, 151 (1987).

4. Narasimhan, R., and Rosakis, A. J., 3-Dimensional Effects Near a Crack Tip in a Ductile 3-Point Bend Specimen. I. A Numerical Investigation, *Journal of Applied Mechanics*, 57, 607 (1990).

5. Sharma, S. M., and Aravas, N., Determination of Higher Order Terms in Asymptotic Elastoplastic Crack Tip Solutions, *Journal of the Mechanics and Physics of Solids*, 39, 1043 (1991).

6. O'Dowd, N. P., and Shih, C. F., Family of Crack Tip Fields Characterized by a Triaxiality Parameter. II. Fracture Applications, *Journal of the Mechanics and Physics of Solids*, 40, 939 (1992).

7. Yang, S., Chao, Y. J., and Sutton, M. A., Complete Theoretical Analysis for Higher Order Asymptotic Terms and the HRR Zone at a Crack Tip for Mode I and Mode II Loading of a Hardening Material, *Acta Mechanica*, 98, 79 (1993).

8. Rosakis, A. J., Zehnder, A. T., and Narasimhan, R., Caustics by Reflection and Their Application to Elastic-Plastic and Dynamic Fracture Mechanics, *Optical Engineering*, 27, 596 (1988).

9. Shih, C. F., Relationships Between the *J*-Integral and the Crack Tip Opening Displacement for Stationary and Extending Cracks, *Journal of the Mechanics and Physics of Solids*, 29, 305 (1981).

ORDER OF MAGNITUDE SCALING OF COMPLEX ENGINEERING PROBLEMS

Patricio F. Mendez and Thomas W. Eagar
Massachussetts Institute of Technology
Cambridge, MA 02139

ABSTRACT

This paper presents a methodology for obtaining order of magnitude estimations of complex engineering problems which are described by differential equations. It is often found that measurements and numerical treatment can be difficult in some of these problems. This might be due to the lack of reliability of idealizations, or the inability of dimensional analysis to reduce the number of arguments significantly. The methodology presented here overcomes these difficulties by bridging the fields of dimensional analysis and asymptotic considerations. The differential equations are transformed into a set of algebraic equations, which are much simpler to solve. The results obtained are estimations of the characteristic values of the unknown functions. It is not necessary to solve the differential equations in order to obtain the estimations; however, previous physical insight is necessary in order to perform the proper normalization and asymptotic considerations. The classical boundary layer problem is studied as a representative example, and it is shown that the estimations obtained are within a factor of 2 of the exact solution.

INTRODUCTION

Dimensional analysis and asymptotic considerations have been linked by some authors before. Barenblatt [1] focused on the application of dimensional analysis to obtain exact asymptotic solutions. Denn [2] introduces a scaling for pressure that depends on whether inertial or viscous forces dominate. He also uses the concept of dominant balance described by Bender *et al.*[4]. Chen [3] is the first to describe some of the properties of the dimensionless functions and their implications; however, he assumes that if the function and its arguments are normalized with their scale, all the dimensionless derivatives are of the order of one. This last statement is not generally valid and there are important cases for which it does not hold true. The order of magnitude methodology presented here applies some of Chen's concepts such as the emphasis on the normalization of the functions and its derivatives. The normalization is based on the scale of the unknown functions (velocity, temperature, etc.). The governing equations are normalized with the dominant terms of the equations. In this work the dominant terms are determined using a variation of the technique of dominant balance. One of the new concepts presented in this research is the requisite of an upper bound for the second derivative (the dimensionless second derivative must be of the order of one, and this implies the partition of the domain in some cases). Another novel concept is the transformation of a system of differential equations

into an algebraic system. This useful simplification is possible by assuring that the unknown functions and derivatives are of the order of one, and their unknown scale is contained in a set of estimations. Also, a number of sets is introduced so matrix algebra can be used to simplify the calculation of the estimations.

Instead of having an abstract discussion, the order of magnitude scaling methodology is presented through an example. This example is the viscous boundary layer, for which the solution is known and can be used as a benchmark of the quality of the estimations obtained.

EXAMPLE: ORDER OF MAGNITUDE SCALING OF THE VISCOUS BOUNDARY LAYER

The objective is to obtain an estimation of the thickness and velocities in the viscous boundary layer. It is assumed that the fluid is incompressible and isothermal, and no external pressure gradients are applied.

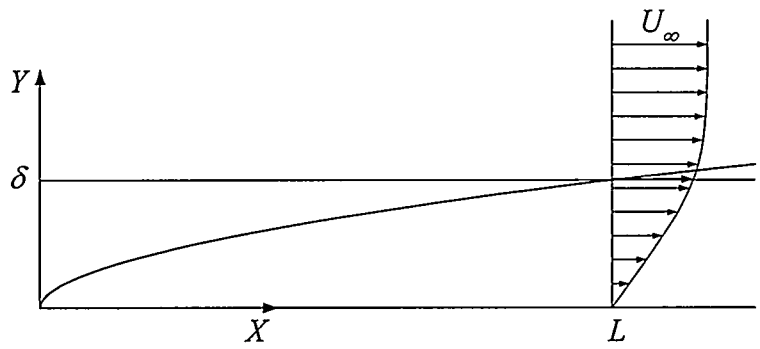

Figure 1: Schematic of the viscous boundary layer and the domain for scaling

Governing Equations, Boundary Conditions, and Domain for Scaling

$$\frac{\partial U}{\partial X} + \frac{\partial V}{\partial Y} = 0 \tag{1}$$

$$U\frac{\partial U}{\partial X} + V\frac{\partial U}{\partial Y} = -\frac{1}{\rho}\frac{\partial P}{\partial X} + \nu\left(\frac{\partial^2 U}{\partial X^2} + \frac{\partial^2 U}{\partial Y^2}\right) \tag{2}$$

$$U\frac{\partial V}{\partial X} + V\frac{\partial V}{\partial Y} = -\frac{1}{\rho}\frac{\partial P}{\partial Y} + \nu\left(\frac{\partial^2 V}{\partial X^2} + \frac{\partial^2 V}{\partial Y^2}\right) \tag{3}$$

The boundary conditions are: $U(X > 0, 0) = 0$, $V(X > 0, 0) = 0$, $U(-\infty, Y) = U_\infty$, $V(-\infty, Y) = 0$, $P(0, \infty) = 0$.

There are two independent arguments: X and Y. The equations are defined for an infinite domain over both independent arguments; however, a finite domain must be defined for the scaling. An arbitrary finite length L is defined as the domain limit in the X-direction. The

domain in the Y-direction will be limited by the characteristic thickness of the boundary layer (δ). Because L is arbitrary, it is a known characteristic value, and belongs to the set $\{P\}$ of parameters that completely determine the problem. The thickness of the boundary layer is unknown, and its estimation ($\widehat{\delta}$) belongs to the set $\{S\}$ of estimations.

Sets of Parameters and Units

The set of parameters that completely determine the problem is obtained by inspection of the system of equations, its boundary conditions, and its domain, this way the complete set of parameters for this problem is:

$$\{P\}^T = \{\rho, \nu, U_\infty, L\} \tag{4}$$

A reasonable choice for the system of units is the SI. The set of reference units $\{R\}$ is obtained by expressing the units of each element of $\{P\}$ in the SI and inspecting the reference units involved:

$$\{R\}^T = \{\text{m, kg, s}\} \tag{5}$$

The matrix of dimensions $[U]^T$ for this problem is shown in Figure 2. Its rank is 3; therefore, three dimensionally independent parameters constitute a set of reference parameters:

$$\{P_k\}^T = \{\rho, \nu, U_\infty\} \tag{6}$$

	ρ	ν	U_∞	L
m	-3	2	1	1
kg	1			
s		-1	-1	

Figure 2: Matrix of dimensions $[U]^T$ for the viscous boundary layer. The submatrix on the left has rank 3, indicating that there are three dimensionally independent parameters

Scaling Relationships, Characteristic Values and Order of Magnitude Estimations

Scaling Relationships for the Independent Arguments

The domain for scaling is the rectangle $0 \leq X \leq L$, $0 \leq Y \leq \delta$, where L is the characteristic value for X, and δ the characteristic value for Y. Because δ is unknown, its estimation $\widehat{\delta}$ is used for the scaling relationships for the independent arguments:

$$X = Lx \tag{7}$$
$$Y = \widehat{\delta} y \tag{8}$$

Scaling Relationship for $U(X, Y)$

For laminar flow, the minimum value of U is 0, and the maximum is U_∞, therefore U_∞ is the characteristic value for U. Previous physical insight in this case comes from the well known

solutions by Blasius [5]. There are no sharp changes in the slope of U inside the domain, therefore $u(x,y)$ and its first two derivatives are of the order of one. The scaling relationship for U then is:

$$U(X,Y) = U_\infty u(x,y) \tag{9}$$

Scaling Relationship for $V(X,Y)$

The transverse velocity V is 0 at the plate and upstream. Previous physical insight indicates that there are no sharp changes in the slope of V inside the domain, therefore $v(x,y)$ and its first two derivatives are of the order of one. The characteristic value of V is V_C, which is unknown; therefore, an estimation will be used in the scaling relationship.

$$V(X,Y) = \widehat{V}_C v(x,y) \tag{10}$$

Scaling Relationship for $P(X,Y)$

The minimum value of P is 0 far from the plate, but its characteristic value P_C is unknown. It is estimated by $\widehat{P}_C$, and the scaling relationship is:

$$P(X,Y) = \widehat{P}_C p(x,y) \tag{11}$$

Based on the scaling relationships defined above, the set of estimations $\{S\}$ is:

$$\{S\}^T = \{\widehat{\delta}, \widehat{V}_C, \widehat{P}_C\} \tag{12}$$

Dimensionless Governing Equations and Boundary Conditions

The original set of equations is normalized by using the scaling relationships and the dominant terms. The dominant terms are determined using a variation of the technique of dominant balance. In this work, a guess for a dominant term is verified by checking that all of the dimensionless coefficients in the equations are lesser or equal to one. The normal formulation for a dominant balance requires that the equations are simplified and solved. Equation 14 (conservation of momentum in the x-direction) was normalized with the viscous forces. This viscous forces create pressures, which are the forces used to normalize equation 15 (conservation of momentum in the y-direction). The expression of the coefficients N_i appears in matrix $[A]$ (Figure 3).

$$\frac{\partial u}{\partial x} + N_1 \frac{\partial v}{\partial y} = 0 \tag{13}$$

$$N_2 u \frac{\partial u}{\partial x} + N_3 v \frac{\partial u}{\partial y} = -N_4 \frac{\partial p}{\partial x} + \left(N_5 \frac{\partial^2 u}{\partial x^2} + \frac{\partial^2 u}{\partial y^2} \right) \tag{14}$$

$$N_6 u \frac{\partial u}{\partial x} + N_7 v \frac{\partial u}{\partial y} = -\frac{\partial p}{\partial y} + N_8 \left(N_5 \frac{\partial^2 v}{\partial x^2} + \frac{\partial^2 v}{\partial y^2} \right) \tag{15}$$

The boundary conditions are: $u(x > 0, 0) = 0$, $v(x > 0, 0) = 0$, $u(-\infty, y) = 1$, $v(-\infty, y) = 0$, $p(0, \infty) = 0$.

Dimensionless Groups of Known Order of Magnitude

The boundary layer is the region where the flow transitions from stagnant (at the wall) to free flow (far from the wall). Close to the wall the viscous forces are dominant, and far from the wall the inertial forces dominate. A practical and physically meaningful way to define the boundary layer (used by Rivas and Ostrach [6]) is as the "region where the viscous forces are of the same order of magnitude as the inertial forces". From this consideration, the group N_3 can be estimated as equal to one. The group N_1 is also estimated as equal to one because it relates two terms that ar of the order of magnitude of one. The group N_4 will also be estimated as one, indicating that the pressure scales with the viscous and inertial forces.

Complete Set of Dimensionless Groups

From Buckingham's theorem it is known that this problem can be described completely by just one non-dimensional group. The Reynolds number ($\mathrm{Re} = U_\infty L/\nu$) is arbitrarily chosen to describe the problem.

Expression of the Estimations

Matrix algebra will be used to illustrate its application, although this problem is simple enough as to be solved by simple inspection. The matrix $[A]$ of dimensionless groups is shown in Figure 3.

	ρ	ν	U_∞	L	$\widehat{\delta}$	$\widehat{V}_C$	$\widehat{P}_C$
N_1			-1	1	-1	1	
N_3		-1			1	1	
N_4	-1	-1	-1	-1	2		1
Re		-1	1	1			
N_2		-1	1	-1	2		
N_5				-2	2		
N_6	1		1	-1	1	1	-1
N_7	1					2	-1
N_8	1	1			-1	1	-1

Figure 3: Matrix $[A]$ for the viscous boundary layer. The internal lines divide the submatrices $[A_{ij}]$. The elements of the matrix are the exponents of the parameters in each dimensionless group

The matrix of estimations $[A_S]$ is shown in Figure 4. It is obtained by using the following equation:

$$[A_S] = -[A_{12}]^{-1}[A_{11}] \tag{16}$$

The expression for the estimation of the boundary layer thickness is obtained from matrix $[A_S]$:

$$\widehat{\delta} = \sqrt{\frac{\nu L}{U_\infty}} \tag{17}$$

Finally, the exact boundary layer thickness is $\delta = \widehat{\delta} g(\mathrm{Re})$, where $g(\mathrm{Re})$ is approximately equal to one.

	ρ	ν	U_∞	L
$\widehat{\delta}$		1/2	-1/2	1/2
$\widehat{V}_C$		1/2	-1/2	-1/2
$\widehat{P}_C$	1		2	

Figure 4: Matrix $[A_S]$ for the viscous boundary layer

Dimensionless Governing Equations and Boundary Conditions (In Terms of the Reference Dimensionless Groups)

Even though an estimation of the characteristic value of the functions in the problem was already obtained, rewriting the equations in terms of the reference dimensionless groups (in this case, the Reynolds number) is useful as a check of consistency and for added physical insight.

$$\frac{\partial u}{\partial x} + \frac{\partial v}{\partial y} = 0 \tag{18}$$

$$u\frac{\partial u}{\partial x} + v\frac{\partial u}{\partial y} = -\frac{\partial p}{\partial x} + \left(\frac{1}{\mathrm{Re}}\frac{\partial^2 u}{\partial x^2} + \frac{\partial^2 u}{\partial y^2}\right) \tag{19}$$

$$\frac{1}{\mathrm{Re}}\left(u\frac{\partial u}{\partial x} + v\frac{\partial u}{\partial y}\right) = -\frac{\partial p}{\partial y} + \frac{1}{\mathrm{Re}}\left(\frac{1}{\mathrm{Re}}\frac{\partial^2 v}{\partial x^2} + \frac{\partial^2 v}{\partial y^2}\right) \tag{20}$$

The equations above are equivalent to their dimensional counterparts, no physical aspects have been neglected or modified. The boundary layer is commonly studied at large Reynolds numbers, because that is the case when it can be considered thin and independent of Re. Inspecting the equations, it can be seen that at values of the Reynolds number larger than one, all term are of the order of one. The term $\partial p/\partial y$ in equation 20 is very small ($\mathrm{O}(\mathrm{Re}^{-1})$), indicating that the pressure gradient is approximately parallel to the x axis.

Comparison with Known Results

The expression of $g(\mathrm{Re})$ can be obtained from the literature [5]. This expression depends on the definition of boundary layer thickness used. The displacement thickness of the boundary layer is an integral definition that can be compared to the definition used here, and at high Reynolds numbers it is where the parallel velocity is 99% of that of the free flow. In this case the dimensionless function would be $g(\mathrm{Re}) = 5$. It is not difficult to try to improve the order of magnitude estimations according to this definition. The thickness of the boundary layer could be estimated as the region where the inertial forces are 100 times larger than the viscous; this statement is translated into $N_2 = 100$, with an estimated boundary layer thickness is $\widehat{\delta} = 10\sqrt{\nu L/U_\infty}$. In this last case, the dimensionless function is $g(\mathrm{Re}) = 0.5$.

DISCUSSION

This technique expands the capabilities of dimensional analysis by incorporating information from previous physical insight and the governing equations. For both standard dimensional

Table 1: Comparison of estimated and exact thickness of the viscous boundary layer for different definitions. It can be observed that the dimensionless function $g(\mathrm{Re})$ is approximately equal to one for all cases.

Definition	Estimation	N_2	δ	$\widehat{\delta}$	$g(\mathrm{Re})$
displacement thickness	inertial forces$\approx$ viscous forces	1	$1.72\sqrt{\nu L/U_\infty}$	$\sqrt{\nu L/U_\infty}$	1.72
$99\%U_\infty$	inertial forces$\approx$ viscous forces	1	$5\sqrt{\nu L/U_\infty}$	$\sqrt{\nu L/U_\infty}$	5
$99\%U_\infty$	inertial forces$\approx$ 100$\times$viscous forces	100	$5\sqrt{\nu L/U_\infty}$	$10\sqrt{\nu L/U_\infty}$	0.5

analysis and order of magnitude scaling, the unknowns are expressed in the form of a power law multiplied by an unknown function of the governing dimensionless parameters; however, in order of magnitude scaling that function is known to be approximately equal to one, while in dimensional analysis that function is unknown, and can have any behavior or order of magnitude.

This methodology can be applied to non-linear equations such as Navier-Stokes. Its present formulation, however, is limited to differential equations of second order or lower; the reason is that it is difficult to assure that lower order derivatives are of the order of one when dealing with higher order equations. Another limitation in the current formulation is that the equations must be written in scalar form, excluding vectorial notation. The reason is that the same vector might need to be assigned more than one scale (for example different scales in the X and Y directions). The circular logic of the dominant balance technique limits the generality of this methodology because not all of the dangerous cases can be identified beforehand. Special precautions should be taken when a dimensionless function can be of an order of magnitude smaller than one. In this case, differential equations might be transformed into into algebraic inequalities, which are difficult to analyze.

Problems for which many domain subdivisions are necessary (in order to reduce the magnitude of the second derivative) are beyond the scope of this methodology because they cannot be simplified significantly. Unstable systems, such as those presenting capillary instability may be of this type.

When using matrix algebra to implement this methodology the matrices involved are generally small, and the matrix operations relatively simple. The calculation process can be performed with commercial software tools.

CONCLUSIONS

Order of magnitude scaling is helpful to the engineer who needs to gain insight into a complex problem but cannot afford to tackle the full solution of the governing equations. The estimations can be obtained without solving the differential equations because the original system of differential equations is transformed into a linear algebraic system. These estimations can be

used to determine the relative importance of the different driving forces in the problem, thus gaining deeper physical insight into it.

The estimations are related to the governing parameters through power laws, and the exact value of the characteristic values is related to the estimations through an unknown function of the governing dimensionless parameters. This function is approximately equal to one, and can be considered as exactly equal to one for order of magnitude approximations.

The approximations obtained can be refined by further calculations or experiments. The knowledge gained regarding what dimensionless groups can be neglected reduces significantly the necessary number of experiments or calculations. The simple expression of the solutions makes them suitable to be implemented in real-time control algorithms. When using matrix algebra to implement this methodology the matrices involved are generally small, and the matrix operations relatively simple. The calculation process can be performed with commercial software tools.

The boundary layer example illustrates the practical implementation of this methodology, and shows that the results obtained match satisfactorily the exact solution to the equations.

This work was supported by the United States Department of Energy, Office of Basic Energy Sciences.

References

[1] G. I. Barenblatt. *Scaling, Self-similarity, and Intermediate Asymptotics.* Cambridge Texts in Applied Mathematics; 14. Cambridge University Press, New York, 1996.

[2] M. M. Denn. *Process Fluid Mechanics.* Prentice-Hall International Series in the Physical and Chemical Engineering Series. Prentice-Hall, Englewood Cliffs, NJ, first edition, 1980.

[3] M. M. Chen. Scales, Similitude, and Asymptotic Considerations in Convective Heat Transfer. In C. L. Tien, editor, *Annual Review of Heat Transfer*, volume 3, pages 233–291. Hemisphere Pub. Corp., New York, 1990.

[4] C. M. Bender and S. A. Orszag. *Advanced Mathematical Methods for Scientists and Engineers.* International Series in Pure and Applied Mathematics. McGraw-Hill, New York, 1978.

[5] H. Schlichting. *Boundary-Layer Theory.* McGraw-Hill classic textbook reissue series. McGraw-Hill, New York, 7th edition, 1987.

[6] D. Rivas and S. Ostrach. Scaling of Low-Prandtl-Number Thermocapillary Flows. *Int. J. Heat Mass Transfer*, 35(6):1469–1479, 1992.

LOW TEMPERATURE TIME DEPENDENT CRACKING

W. A. Van Der Sluys

J. M. Bloom

McDermott Technology Inc.

ABSTRACT

This paper describes a project to investigate metallurgical and mechanical phenomena associated with the occurrence of piping failures in fossil boilers due to time dependent cracking. These failures occur in carbon steels piping at temperatures between 320C and 360C. Time dependent cracking failures of carbon steel piping in this temperature range have been experienced in the fossil power industry for almost thirty years. The information developed in this project will aid in the development of more comprehensive materials specification that will eliminate the possibility for this type of failure in the future.

INTRODUCTION

This paper describes a project to investigate metallurgical and mechanical phenomena associated with the occurrence of piping failures in fossil boilers due to time dependent cracking. These failures occur in carbon steels piping at temperatures between 320C and 360C. Time dependent cracking failures of carbon steel piping in this temperature range have been experienced in the fossil power industry for almost thirty years. Moreover, these failures can occur suddenly, creating a serious threat to human safety and substantial monetary losses. Several worldwide research programs conducted to address this problem have demonstrated that failures are proceeded by a creep crack growth mechanism. However, recent field failures suggest that our understanding of the fundamental metallurgical and mechanical parameters controlling this type of failure is still insufficient to eliminate the failures.

BACKGROUND

In the early 1970's, time dependent cracking at the extrados of cold bent elbows resulted in unexpected, catastrophic failures in the piping systems of a number of fossil power utilities around the

world. Failures occurred within the plants of at least five U.S. utilities and it has been reported that failures have occurred within at least twelve European utilities[1]. These failures typically caused significant damage to the boiler facility.[2] Most importantly, cracking often culminated in 'blow-outs' of sections of the elbows, producing a serious threat to human safety. A picture of one of these blown out widows is presented in Fig. 1.

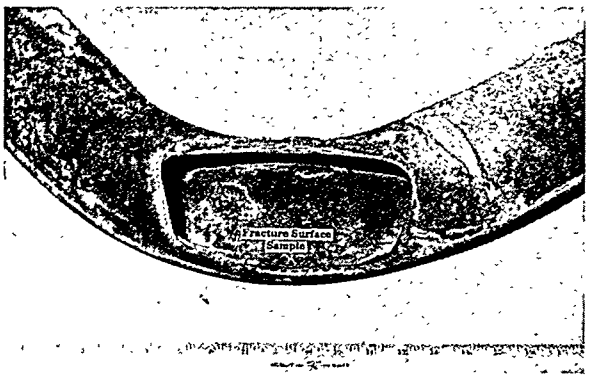

Fig. 1 Picture of failed elbow

This paper describes a project to investigate metallurgical and mechanical phenomena associated with the occurrence of piping failures in fossil boilers due to time dependent cracking. These failures occur in carbon steels piping at temperatures between 320^{oC} and 360^{oC}. Time dependent cracking failures of carbon steel piping in this temperature range have been experienced in the fossil power industry for almost thirty years

Significant resources have been dedicated to characterizing the problem and defining economic means for eliminating this problem. Investigations were independently performed within the U.S. and Europe, but there was no common resolution to this problem. However, the studies in Europe did reveal a number of distinct features that were common to most failures[3]: (1.) Cracking failures occurred in cold-formed material manufactured from common grades of boiler pipe, i.e. SA106 Grade C and SA210 Grade C. (2.) The operating temperature of the failed components was in the range of 300C to 420C. (3.) Failures usually occurred before 10,000 hours of operation, but several were noted at times up to 100,000 hours of operation. Usually the longer lives were attributed to straight pipe sections while the shorted lives were entirely elbows. (4.) Cracking always occurred at the extrados of the bends. (5.) Cracking was typically associated with the presence of small surface defects that were within the limits of the inspection criteria - i.e., laps, seams, hammer marks, gouges, etc. (6.) Stable cracking occurred by an intragranular mode before transitioning to a transgranular mode during final fracture.

Most of the failures, which have occurred in the United States, occurred in the early 1970's. In the U.S. steps were taken in the mid 1970's to limit the stress on the elbows, eliminate defects, and to improve the uniformity of the steels used to fabricate the elbows. This appeared to have eliminated the problems. In Europe failures continued and a large research project was performed in Europe that identified the failure mechanisms identified below. In Europe most of the failures have been eliminated by reducing the stress, eliminating the defects and eliminating the high free nitrogen in the steel. The elimination of elbows with high free nitrogen in the steel is quit costly. Free nitrogen is very hard to measure in the field and if high free nitrogen is detected the only fix is to replace the elbow.

More recently, it has been reported that Indian boiler tube failures account for a power generator loss on 3100 MW Which is equivalent of an annual power generator on one 500 MW Unit at a 70% power loading. During 8 occasions riser tube failures resulted in forced shut down of the power grid. Their study showed the mechanism to be creep crack growth. Temporary fixes reflecting European research studies were stress relief, improved NDE, and control of the free nitrogen.

In the U.S. there were two failures in the early 1990's. These failures were slightly different from the others. The elbows had high residual and tramp element contents. The steel used to fabricate these elbows had been manufactured in Europe and although the steel met the U.S. Code requirements for this

grade of steel the failed elbows contained much higher levels of residual and tramp elements than is typically found in steel manufactured in the U.S. These recent failures raises the concerns that a better understanding of the physical metallurgical and mechanical aspects of these failures is needed. In addition these recent failures raise concerns about the adequacy of U.S. Code material specifications when the materials are manufactured overseas and the manufacturing practices are substantially different from those in the U.S.

Mechanisms

Research on this issue demonstrated that metallurgical conditions which produce good creep rupture strength in carbon-manganese piping steels typically produce poor creep crack growth resistance[5,6,7,8]. The cause is believed to be related to the relative strength of the matrix and grain boundaries in the temperature range of 300C to 420C. When a crack is introduced into a material, the high strain fields ahead of the crack tip cannot be easily accommodated, if the material matrix has high creep strength. As a result, weakening of the grain boundaries by any mechanism can produce cavitation and cracking along the boundaries. This material model agrees well with the observation that these types of failures occur only over a limited temperature range. At lower temperatures, creep mechanisms on the grain boundaries are not operable so cracking does not occur. At higher temperatures, the strength of the matrix is sufficiently reduced to allow accommodation of the crack tip strains. This is also consistent with the small numbers of failures for the large numbers of carbon steel cold bent elbows that are in service. Failures appear to require both a matrix strengthing and a grain boundary weakening mechanism to exist at the service temperature.

There are a variety of phenomena that can contribute to either strengthening of the matrix or weakening of grain boundaries. For example, free nitrogen, residual alloying elements and austenitizing temperatures can strongly impact the matrix strength. Tramp element levels, grain size, and unfavorable distributions of microstructural phases can each influence the propensity for grain boundary cracking and decohesion to occur. These parameters comprise the primary metallurgical factors that will impact the creep crack growth resistance of a C-Mn steel. However, according to Gooch et al.[9], there are a number of engineering factors that will also have an impact on the probability for failure, such as the constraint of the material at a crack tip. It has been observed that constraint influences the materials resistance to creep crack growth (i.e., specimen geometry, specimen size, crack depth, etc.). All of the parameters cited above must be considered when evaluating the propensity for cracking in the field when using laboratory data.

A considerable amount of research has been performed on this topic. Still, the amount of creep crack growth data on these materials is limited[7]. Consequently, a number of unresolved issues remain that demonstrate that a more fundamental understanding of the problem must be obtained before steps can be taken to eliminate this problem from the field.

It has been demonstrated on a limited basis that creep crack growth rate test data can be used to reasonably predict the life of low carbon steel elbows[9]. However, the data from conventional, deeply cracked (a/W>0.4) compact specimens produce results that under-predict the observed failure lives of carbon steel elbows, sometimes by as much as a factor of 10. Deeply notched specimens can produce highly conservative creep crack growth rate data due to the high crack tip constraint associated with the deep notch. This has a direct influence on the damage mechanism and therefore, will influence the crack tip parameter C*, which characterizes the creep crack growth behavior. In fact, some tests using deeply notched specimens have shown that creep crack growth rates can be better correlated to the linear elastic stress intensity factor, K_I. Using the crack growth rate / K_I correlations to predict remaining life in the field produces overly conservative life estimates.

It appears that this relates to whether a material is behaving in a creep-brittle of creep-ductile manor. Creep-ductile materials where the creep rate displacement is large compared to the total displacement rate while creep-brittle materials the creep rate displacement is small compared to the total displacement rates. There is little work on the effect of constraint on the creep-brittle versus creep-ductile behavior. However, the state of stress present in laboratory specimens typically used to study creep crack failures is not representative of the stresses that will exist in the field, at least in the early stages of crack growth. This issue will impact the measured creep crack growth rates and may influence the creep-ductile versus creep-brittle behavior of the specimen.

Failure of the pipe elbows in the field has typically been related to the existence of shallow defects on the pipe extrados that passed inspection at the beginning of service. The flaws range from seams or laps from the pipe manufacturing process to relatively blunt gouges or hammer marks. Studies of field failures indicate that the stresses on the pipe extrados are sufficiently high that any type of measurable flaw produces enough stress concentration to initiate creep crack growth early in the life of the elbow.

ASTM E 1457-98 recommend uses of the compact (CT) specimen under constant load for determine creep crack growth for both creep-ductile and creep-brittle materials. However, it is suggested that constant displacement or displacement rate testing may be more suitable for creep-brittle materials. It is also through that the single edge cracked specimen in tension with a shallow flaw will best simulate the cold bent pipe constraint. For this reason the shallow cracked single edge notched under displacement control is being used in this program.

Additionally, recent progress on theoretically quantifying in-plane constraint for creep crack growth under widespread creep conditions using the Q stress parameter will be incorporated into an existing computer code developed by B&W. Predictions of actual failed lives will be made using laboratory crack growth rate measurements in the more realistic constraint model. The predictions will be compared to actual field lives to assess the effectiveness of accounting for crack tip constraint. B&W feels that this approach is most promising because damage models for fracture of the process zone based on both the ductility exhaustion model and stress rupture model will predict a variation of crack growth with constraint (as measured by the parameter Q).

DESCRIPTION OF CURRENT PROJECT

The work cited in the above Background, has demonstrated that classical creep is operative in C-Mn piping steels (as well as low alloy steels) in the temperature range of 320^{o}F to 360^{o}F; which was previously thought to be too low for creep to occur[4,6,8]. Moreover, widespread creep damage such as that observed in rupture tests is not responsible for the time dependent cracking failures of C-Mn steels observed in the field. The generally accepted mechanism for these failures is believed to be related to a critical combination of creep strength of the metal matrix, decohesion strength of the grain boundaries, and level of constraint at the crack tip. When the critical combination occurs, high levels of crack tip constraint inhibit creep relaxation of the large strains ahead of a crack tip and these crack tip strains encourage separation along prior austenite grain boundaries.

Although a failure mechanism has been defined for the pipe elbow failures, a fundamental understanding of the critical metallurgical/mechanical factors required to produce field failures has not been completely determined. Thus, the purpose of this project is to conduct experimental studies of common grades of piping steels that are designed to elucidate the metallurgical phenomena that contribute to time dependent cracking failures. The expected result of this project is to define mechanical and metallurgical conditions associated with creep crack growth in these types of steels. This information will

be evaluated with respect to steel-making practices, forming operations, heat treating and field conditions to determine the most effective method for eliminating the cracking problems in the field.

The project is being performed in several phases, with each phase building on the results of previous phases. Descriptions of each phase are provided below.

Selection and Baseline Characterization of Test Material

The rate of occurrence of field failures indicates that a critical combination of conditions must exist in a pipe bend for time dependent cracking to occur. Supporting this, previous experimental work has shown that different heats of the same steel grade have different susceptibilities to this type of cracking[5]. Considering that the manufacturing methods were similar between the heats studied in reference 5, and the global properties such as microstructure and hardness were nearly identical, the difference is postulated to lie in compositional differences between the heats - specifically in the free nitrogen, residual alloying element and tramp elements. Thus, materials wee obtained which possess sufficient variations in composition to allow testing of the relative impact of these elements on creep crack growth susceptibility.

Pipe samples of SA106 Grade C and/or SA210 Grade C from various sources. Sufficient materials representing significant compositional variations were obtained for testing. The desired compositions are shown in Table 1.

Table 1 Material Compositions

Si Killed Steels (High nitrogen levels)	**AL Killed or Al treated Steels (Low nitrogen levels)**
Clean (1)	Clean (3)
High residuals and tramp element content (2)	High residuals and tramp element content (4)

The following steps were followed to find samples of pipe with the compositions shown in Table. 1

1. Contacted all U.S. boiler manufactures looking for compositions desired and examples of failed pipe.
2. Performed a survey of B&W R&D archives looking for samples of failed pipe.
3. Searched the inventory of pipe available at B&W manufacturing sites.
4. Contacted Italian and Spanish boiler manufactures for samples of failed pipe.
5. Contacted the Project leader of the European program for failed samples.
6. Checked with tube vendor on available piping with desired compositions.

The results from this effort were that there were no offers of pipe from other manufactures either in the U.S. or overseas were received. An offer was received from the chairman of the European program of 4 samples of pipe material. Five candidate materials in R&D Division storage and four candidate materials from B&W manufacturing sites. However, only one of these samples was from a pipe that had failed in service.

Detailed chemical analyses were conducted on the nine candidate materials found at B&W. The compositions of these nine materials and the four materials offered from Europe were then reviewed and four materials were selected for the test matrix.

Table 2 contains the results of chemical analysis of the four heats of material. Of particular interest are the two "dirty" heats of material. These two heats are of the most interest in the test program.

Table 2 Composition of the test materials

Standard elements

Material	C w%	Mn w%	S w%	P w%	Si w%	Cr w%	Ni w%	Mo w%	Cu w%	N w%	Al w%
Heat M (1)	0.25	0.46	0.021	0.007	0.18	0.1	0.1	0.04	0.05	0.0055	0.011
Heat D (2)	0.26	0.68	0.01	0.008	0.24	0.15	0.11	0.02	0.22	0.011	0.004
A42425 (3)	0.18	1.05	0.007	0.006	0.23	0.05	0.02	0.02	0.01	0.0047	0.021
Heat 98541 (4)	0.19	0.75	0.007	0.006	0.33	0.04	0.06	0.02	0.16	0.006	0.024

Trace elements

Material	CR w%	Ni w%	Mo w%	Cu w%
M	0.1	0.1	0.04	0.05
Heat D	0.15	0.11	0.02	0.22
A42425	0.05	0.02	0.02	0.05
Heat 98541	0.04	0.06	0.02	0.16

Tamp elements

Material	P w%	S w%	Cu w%	Sn w%	Sb w%	As w%
Heat M	0.007	0.021	0.05	0.005	0.0018	0.007
Heat D	0.008	0.01	0.22	0.015	0.0037	0.015
A42425	0.006	0.007	0.05	0.001	0.006	0.0024
Heat 98541	0.006	0.007	0.16	0.014	0.003	0.0089

In order to cold work the material, it was originally planned to bend the pipe to the same degrees as the field bends which failed. The amount of strain typical in the failed bends is from 20 to 25% strain. It is impossible to strain this material in a uniaxial tension test to achieve a uniform strain of this amount. The tension specimens will experience necking at strain levels of 15 to 16%. Not enough pipe could be obtained of the materials of interest to use this method of cold work. Since only the exrados of the bend receives the desired cold work strains, only a small portion of the pipe bend can be used. It was decided to attempt to develop a tension specimen with enough biaxial constraint to achieve the desired strain levels. Tension tests were conducted on one of the candidate heats. The stress strain curve was used in an elastic plastic finite element model of a flat plate tension specimen in order to optimize the proportions of the specimen. Three specimens were then machined. One specimen of the optimal proportions from the finite element analysis, one with a slightly longer gage length, and a third with an even longer gage length were machined. These specimens were then loaded with a superimposed grid pattern and the strain distribution determined. The middle specimen of the three appeared to give an acceptable strain distribution. Four tension or creep specimens or one creep crack growth specimen can be machined from each of the cold worked specimen.

Material characterization matrix

Tension tests and primary creep test are being conducted on each of the 12 material conditions shown in Table 3. Tension tests are being conducted at both room temperature and 340 C on these materials. Primary creep rate testing will also be conducted at four stress levels and at 340 C on each of the 12 materials. The microstructure of the creep specimens will then be extensively studied to obtain information on the effect of the applied stress and cold work on the matrix strengthening mechanisms in the four materials. The composition of the grain boundaries will also be studied looking for indications of grain boundary weakening mechanisms. Extensive use of electron optics will be made in this work. SEM AUGER TEM and perhaps STEM will be employed in this study.

At this time the cold working of the more than 40 tension specimens is underway.

Table 3. Test materials for Tension and creep testing

Material	Material condition
Low Al /N, low residuals	High cold work
Low Al /N, low residuals	High cold work + SR
Low Al /N, low residuals	High cold work + N
High Al/N, low residuals	High cold work
Low AL/N, high residuals	AR
Low AL/N, high residuals	Med. cold work
Low AL/N, high residuals	High cold work
Low AL/N, high residuals	High cold work + SR
Low AL/N, high residuals	High cold work + N
High Al N, high residuals	High cold work
High Al N, high residuals	High cold work + SR
High Al N, high residuals	High cold work + N

Creep Crack Growth Matrix

Creep crack grow testing will be performed using a single end notch tension specimen under displacement loading at 340C. Three specimens will be tested of each of the materials in Table 4. This test procedure is under development. The equations for the calculation of C^* are not included in the ASTM test method for creep crack growth we are developing the needed equations.

Table 4 Test materials for creep crack growth testing

Material	Material condition
Low Al /N, low residuals	High cold work
Low Al /N, low residuals	High cold work + SR
Low Al /N, low residuals	High cold work + N
High Al/N, low residuals	High cold work
Low AL/N, high residuals	AR
Low AL/N, high residuals	Med. cold work
Low AL/N, high residuals	High cold work
Low AL/N, high residuals	High cold work + SR
Low AL/N, high residuals	High cold work + N
High Al N, high residuals	High cold work
High Al N, high residuals	High cold work + SR
High Al N, high residuals	High cold work + N

After the creep crack growth testing and the metallurgical analysis of the creep specimens has been completed interrupted creep crack growth tests are planned on one of the test materials. The material in the plastic zone at the tip of these specimens will be extensively studied again using the tools of electron

optics. In addition it will be attempted to fails some small specimens intergranularly in an auger electron spectrometer so that the grain boundary composition can be determined.

References

1. W. R. Apblett, Jr., "Reasons For and Prevention of Riser and Feeder Failures in LargeUtilityTypeBoilers",Foster Wheeler Report FWC/RN-247, May 1981.
2. "B&W Asks Customers to Inspect Boiler Tubing After Series of Failures", Electrical World Week, December 28, 1970.
3. M. Prager, Minutes of Materials Property Council Workshop on "Mechanisms and Causes of Cracking in Carbon and Low Alloy Steel Boiler Piping at Intermediate Temperatures", held in conjunction with the ASME Pressure Vessel and Piping Conference, June 1991.
4. I. A. Shibli, "Investigation of a Failure Problem in Cold-Bent Boiler Riser and Supply Pipes", International Journal & Pressure Vessel and Piping, 24, 1986, pp. 303-336.
5. I. A. Shibli, "Creep Crack Growth Characteristics of Pre-Strained C-Mn Steels at 360 C", Materials Science and Technology, 3, February 1987, pp. 110-117.
6. D. J. Gooch, "The Effect of Cold Work on Low Temperature ($0.35T_m$) Creep Crack Growth in C-Mn Steels", Materials Science and Engineering, 64, 1984, pp. 183-196.
7. D. J. Gooch, "The Effect of Microstructure on Creep Crack Growth in a C-Mn Steel at 360 C", Materials Science and Engineering, 83, 1986, pp. 17-27.
8. G. J. Neate, "Creep Crack Growth in Cold Formed C-Mn Steel at 360 C", Materials Science and Technology, 3, 1987, pp. 14-22.
9. D. J. Gooch, J. R. Haigh and B. Liking, "Relationship Between Engineering and Metallurgical Factors in Creep Crack Growth", Metal Science, November, 1977, pp. 545-550.

THREE-DIMENSIONAL FRACTURE MECHANICS COMPUTATIONS USING TETRAHEDRAL FINITE ELEMENTS

D. M. Parks, H. Rajaram and S. Socrate

Department of Mechanical Engineering
Massachusetts Institute of Technology, Cambridge, MA 02139, USA

Abstract

With the development of CAD packages which can create complicated 3-D models and mesh them with tetrahedral elements with relative ease, the application of finite element techniques in mechanical design has reached unprecedented proportions. However, the extension of these techniques to fracture mechanics studies is hindered by the unavailability of a general method to obtain fracture mechanics singularity strength (J, K_I, etc.) for tetrahedral meshes. An approach to obtain these parameters along a 3-D crack front using tetrahedral elements is presented here. The method is then validated on well-known crack geometries using tetrahedral meshes generated from commercially-available CAD-FEA packages.

1 Introduction

The overall quality of mesh generators for tetrahedral elements has been consistently improving over the past decade, and a number of CAD-FEA interfaces are now available, thus allowing construction of complicated 3-D models at the click of a button. However, currently-available finite element implementations of domain integral or virtual crack extension methods for evaluating the variation of fracture mechanics singularity strength (J, K_I, etc.) along a 3-D crack front require the use of brick elements in the neighborhood of the crack. Unfortunately, the capabilities of mesh generators for brick elements remain in a comparatively early stage of development [1]. In order to address this issue, we extended domain integral techniques to tetrahedral meshes. A "straightforward" implementation of the method proved quite unsatisfactory; the estimated nodal J-values along the crack front depended strongly on the particular choice of the perturbation field and were in poor agreement with analytical predictions. Refining the tetrahedral meshes and optimizing element aspect ratios did not result in substantial improvements. These difficulties are tied to the inability of the quadratic tetrahedral shape functions to describe accurately the gradients introduced by a node-based representation of the perturbation fields.

In the approach proposed here, we have overcome the poor performance of the tetrahedral shape functions while remaining within the framework of the finite element method. We selectively evaluated the perturbation gradient at the integration points of the elements in the interior of the domain through direct analytical differentiation of the globally-defined perturbation field, while we retained the shape function representation of the perturbation gradient for elements on the boundary of the domain. The versatility of finite elements in modeling crack combinations and free surface configurations was thus preserved. This simple expedient has allowed us to improve dramatically the accuracy of the procedure, as demonstrated by validation on a number of standard crack configurations.

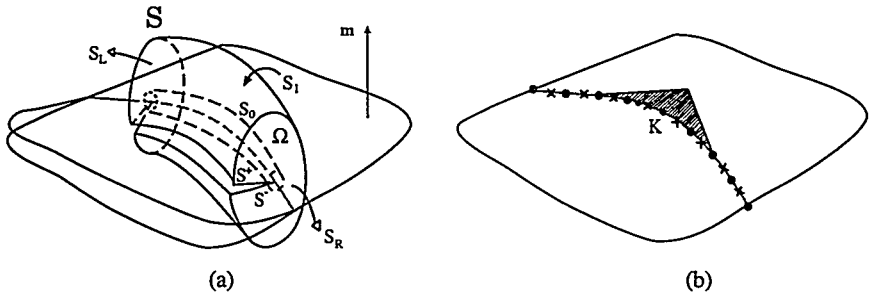

Figure 1: Three-dimensional formulation of the domain integral method. (a) Domain of integration. (b) Crack-front perturbation pattern $\delta l^K(s)$.

2 Formulation and finite element implementation of the proposed method

A brief outline of the proposed method is presented here. A detailed formulation and the finite element implementation of the method can be found in [2].

2.1 Domain integral method

The path-independent J-integral is a measure of the intensity of the singular crack-tip fields which can be used to correlate the initiation of crack propagation. The J-integral also characterizes the energy release for a virtual crack extension. For a virtual crack advance $\delta l(s)$ in the plane of the crack and in the direction normal to the crack-front, we can express, to within first-order terms,

$$\int_C J(s)\delta l(s)ds = -\delta\pi, \tag{1}$$

where s is the curvilinear coordinate along the crack-front C, ds is the elemental arc length along C, and $-\delta\pi$ is the decrease in total potential energy of the body.

To develop the three-dimensional formulation of the domain integral method, we consider a three-dimensional, simply-connected domain Ω between surfaces S_0 and S_1, as shown in figure 1 (a). The domain Ω is bounded by the closed surface S formed by the surfaces S_0, S_1, S^+, S^-, S_R and S_L, where S^+ and S^- are surfaces on the respective crack faces, and S_R and S_L are the respective ends of the cylindrical domain. We now define a perturbation field $\mathbf{q}$, in Ω as $\mathbf{q} \equiv 0$ on $S_1 \cup S_R \cup S_L$; $\mathbf{q} \equiv \delta l(s)\mathbf{n}(s)$ on C and $\mathbf{q} \cdot \mathbf{m} = 0$ on $S^+ \cup S^-$, where $\mathbf{n}$ is the in-plane normal at location s and $\mathbf{m}$ is the normal to the crack plane. The domain integral expression for the energy release can be obtained using the $\mathbf{q}$-field in Ω as

$$-\delta\pi = \int_\Omega [W\delta_{kj} - \sigma_{mj}\frac{\partial u_m}{\partial x_k}]\frac{\partial q_k}{\partial x_j}dV. \tag{2}$$

2.2 Finite element implementation

For a crack-front comprised of N nodes, to obtain values of the J-integral at nodes along the crack-front, we define $N_J = (N+3)/4$ perturbation patterns centered on every alternate corner node along the crack-front. We extend the base of each perturbation pattern to span four adjacent crack-front element-edges, as shown in figure 1 (b). This differs significantly from a "straightforward" implementation of the domain integral method where the perturbations are based on quadratic shape functions for every node on the crack-front. While no perturbation fields are centered at the mid-side nodes in our implementation, the mid-side nodes are still used in order to obtain accurate deformation fields and to accurately define curved crack-fronts.

This expedient has led to a tremendous improvement in the accuracy of the computed J. For each of the N_J perturbation patterns, $\{\delta l^1(s), .., \delta l^K(s),.., \delta l^{N_J}(s)\}$, we can obtain N_J values of J along the crack-front $\{J_1, .., J_K, .., J_{N_J}\}$. For the $K-th$ perturbation pattern $\{ \mathbf{q}^K; \delta l^K(s); \Omega^K \}$, we have a crack-front integral expression for the energy release:

$$\delta\pi^K = -\int_C J(s)\delta l^K(s)ds, \tag{3}$$

as well as the corresponding domain-integral expression:

$$\delta\pi^K = -\int_{\Omega^K}[W\delta_{kj} - \sigma_{mj}\frac{\partial u_m}{\partial x_k}]\frac{\partial q_k^K}{\partial x_j}dV. \tag{4}$$

Equation (4) is evaluated via element-by-element numerical quadrature over Ω^K. To evaluate (4), we divide the domain Ω^K into a core domain $\tilde{\Omega}^K$, and a periphery domain, $\bar{\Omega}^K$. For elements within the core domain $\tilde{\Omega}^K$, we evaluate the gradients of the $\mathbf{q}^K$-functions, at each integration point, analytically. For elements within the periphery domain $\bar{\Omega}^K$, we evaluate $\partial q_i^K/\partial x_j$ based on the value of the $\mathbf{q}^K$-field at the four corner nodes, and use linear shape functions to interpolate $\mathbf{q}^K$, so that the resulting perturbation gradient is constant over the element. This method overcomes undesirable effects linked to the interpolation of the perturbation gradient by the quadratic tetrahedral shape functions in a "straightforward" implementation, and leads to a significant improvement in the accuracy of the results.

Equations (4) and (3) are equivalent representations of the energy release associated with the K-th perturbation pattern. Equating the RHS of (4) and (3) for each pattern of perturbation, we obtain a system of N_J equations in N_J unknowns J_I,

$$[A_I^K]\{J_I\} = \{\delta\pi^K\}. \tag{5}$$

Solving the system of equations (5) gives the nodal values of the J-integral.

2.3 Elastic-plastic formulation

Many problems in crack plasticity are solved by considering the deformation as non-linear elastic through the deformation theory of plasticity. However, in most cases for purposes of elastic-plastic fracture mechanics computation, the incremental theory of plasticity and the deformation theory are equivalent. We can express the energy density W, used in the definition of J as

$$W(\epsilon_{kl}) = \int_0^{\epsilon_{kl}} \sigma_{ij}(d\epsilon_{ij}^e + d\epsilon_{ij}^p) = W^e(\epsilon_{kl}) + W^p(\epsilon_{kl}), \tag{6}$$

where $d\epsilon_{ij}^e$ and $d\epsilon_{ij}^p$ are the elastic and plastic parts of the total incremental strain $d\epsilon_{ij}$ respectively, W^e is the elastic strain energy, and W^p is the plastic dissipation. Hence, we obtain the volume integral expression for the energy release for the elastic-plastic case from (2) as

$$-\delta\pi = \int_\Omega [(W^e + W^p)\delta_{kj} - \sigma_{mj}\frac{\partial u_m}{\partial x_k}]\frac{\partial q_k}{\partial x_j}dV. \tag{7}$$

To compute the J-values along the crack front, we use the finite element implementation of the domain integral method exactly as described above. The crack-front integral expression remains the same as (3). The volume integral expression for the energy release is now evaluated using (7). The evaluation of (7) is similar in all respects to FE evaluation of (4), except that now both W^e and W^p have to be read at the integration points of the 3-D elements in the domain Ω.

3 Elastic analysis

The proposed method is validated on well-known crack geometries [4]. Solutions for three representative crack-geometries are detailed here. Commercially-available packages ABAQUS/Pre and Pro/MESH were used to create the meshes, and ABAQUS/Standard was used as the FE solver. Two tetrahedral meshes, a regular mesh from ABAQUS/Pre and an irregular mesh from Pro/MESH, were created for each of the crack geometries, and the method was validated on both the meshes. The tetrahedral mesh results were compared to predictions obtained with brick meshes of comparable mesh density, using the domain integral option in ABAQUS/Standard.

3.1 Semi-elliptical surface crack in a finite-thickness plate

Surface cracks are an important class of crack geometries which are crucial to life prediction in aircraft, pressure vessels and other structures. Typically, surface cracks propagate sub-critically by fatigue, with semi-elliptic or near-semi-elliptic crack fronts. A crack with a semi-elliptical front has varying local radius of curvature along the crack front, thus representing a good test to assess the performance of the proposed method on a general 3-D curvilinear crack-front in space. Hence, a planar semi-elliptical surface crack is considered here to validate the accuracy of the method. A comparison of the relative user-time needed to generate brick, regular and irregular tetrahedral meshes for this geometry is shown in table 1. For this relatively simple 3-D crack configuration, a reduction factor between 15 and 20 is evident for automatic tetrahedral meshing; the speed-up factor for more complex geometries can be much larger.

Newman and Raju [3] have obtained stress-intensity factors from detailed finite element models of semi-elliptical surface cracks using a nodal force method. Here, a semi-elliptical surface crack with aspect ratio $a/c = 1/3$ and maximum relative depth $a/t = 0.5$ is considered for analysis. The crack is subjected to uniform remote tension in Mode-I loading. Displaced meshes of the FEM models for the elliptical surface crack are shown in figure 2. The stress intensity factor K_I, at any point ϕ along the semi-elliptical crack, can be expressed as

$$K_I = \sigma^{\infty} \sqrt{[(\pi \frac{a}{Q})]}\, F(\frac{a}{t}, \frac{a}{c}, \phi), \tag{8}$$

where σ^{∞} is the applied stress, a is the crack depth, ϕ is the parametric angle of the ellipse, Q is the shape factor of an ellipse and is given by the square of the complete elliptical integral of the second kind; for $(a/c) = 1/3$, $Q = 1.123$. The value of the boundary correction factor F for the specific crack geometry ($a/c = 1/3$ and $a/t = 0.5$) is obtained as a function of ϕ from Raju and Newman [3]. Results from the FEM models using brick elements, regular and irregular tetrahedral elements, along with the reported values of Newman and Raju, are shown in figure 3, using $(1 - \nu^2)K_I^2 = EJ$. The maximum value of K_I occurs at $\phi = \pi/2$, in agreement with Newman and Raju observations. The average value of the K_I-solution agreed to within 2% of Newman and Raju's findings (which have been reported to be accurate to $1 - 3\%$ [3]), and the oscillations were within 2% and 4% of the mean value for the regular and irregular tetrahedral meshes, respectively.

4 Elastic-plastic analysis

4.1 Edge-cracked model in plane strain

A straight through-thickness crack was considered in a body with characteristic dimensional ratios $(a/B) = 0.5$, $(h/B) = 3.0$, and $(a/w) = 0.5$, as shown in figure 4. The model was constrained to plane strain boundary conditions. The main aim of this elastic-plastic study was to note the accuracy of the method

MESH	USER MESH GENERATION TIME	NUMBER OF NODES
Unstructured tetrahedral mesh (Pro/MESH)	30 minutes	6352
Structured tetrahedral mesh (ABAQUS/Pre)	8 hours	4298
Brick mesh (ABAQUS/Pre)	7.5 hours	4198

Table 1: Approximate total user mesh generation time and size of the problem for the semi-elliptical surface crack in a finite thickness plate.

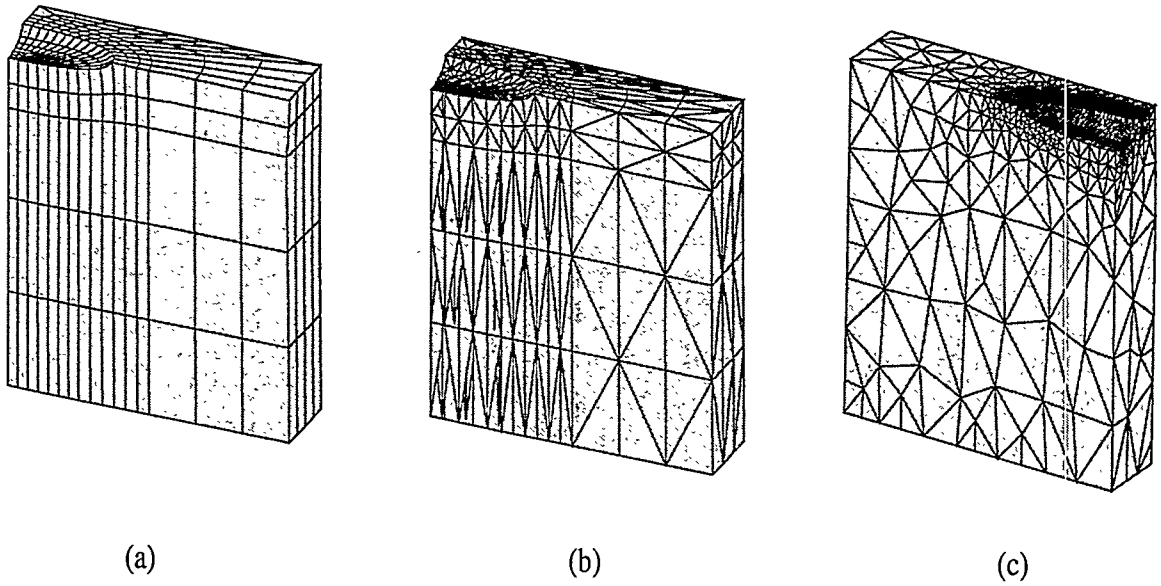

(a) (b) (c)

Figure 2: Displaced meshes of the elliptical surface crack in a finite thickness plate. The models are subjected to uniform remote tension. One-quarter of the plate is modeled. (a) Brick mesh. (b) Regular tetrahedral mesh obtained from ABAQUS/Pre. (c) Irregular tetrahedral mesh obtained from Pro/Mesh.

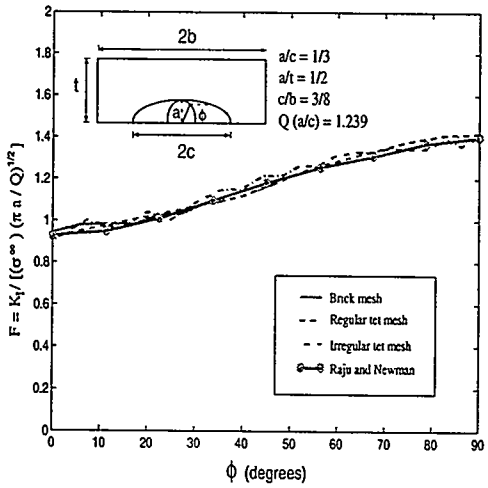

Figure 3: Point-wise J-integral values for semi-elliptical surface crack in a finite thickness plate. The semi-elliptical crack is subjected to uniform remote tension of magnitude σ^{∞}.

in obtaining J-values under fully-plastic conditions. The analysis was performed on an elastic/perfectly-plastic material model with $Y/E = 0.0011$, using the incremental theory of plasticity. The model was loaded with a far-field uniform relative displacement Δ. One-half of the specimen geometry was modeled, and second-order isoparametric (10-noded) tetrahedral elements were used to mesh this geometry with quarter-point elements at the crack tip. A finer mesh was used near the crack to capture the steep crack-tip gradients. The results were also compared with a 2-D plane strain analysis using 2-D 8-noded quadrilateral plane strain elements with reduced integration (CPE8R) from ABAQUS/Standard. The 2-D mesh was also focussed at the crack tip.

The half-specimen was loaded with a far-field displacement of $\Delta/2$. For a rigid-plastic model in plane strain, the limit load P_{LIM} from limit analysis is given by

$$P_{LIM} = \frac{2Yw}{\sqrt{3}}(B-a), \tag{9}$$

where Y is the tensile yield strength of the material, a the crack length and B, w are dimensions as shown schematically in figure 4. From the formal definition of J as the energy difference and for a rigid-plastic formulation, we have

$$\frac{dJ_{Plastic}}{d\Delta} = -\frac{\partial P_{LIM}}{w\,\partial a} = \frac{2Y}{\sqrt{3}}. \tag{10}$$

Hence, the slope of the J-Δ curve is constant in the fully-plastic, non-hardening regime, and this can be used to verify the FE results.

The values of J obtained are normalized using EJ/Y^2a, and the far-field displacement Δ is normalized to $E\Delta/Yl$, where E is the Young's modulus, Y the yield strength, and $l = (B-a)$ is the ligament length as shown in figure 4. The J-profile along the crack-front is shown in figure 4 (a) for three domains of integration at the last increment of loading (*i.e.*, at $E\Delta/Yl = 32$), corresponding to the fully plastic case. The values of J are normalized by the J obtained from the 2-D plane strain solution at the same load-level (*i.e.*, at $E\Delta/Yl = 32$). We observe some path dependence of the computed J-values along the crack-front for the domain close to the crack tip (*i.e.*, $\rho/a = 0.4$, $\rho/a = 0.5$ and $\rho/a = 0.6$). This is because of the basic nature of the incremental theory of plasticity and is discussed in [4]. In our further analysis, for the 3-D meshes, we consider the average value of J along the crack-front, $\bar{J} = \int J dx/w$, to represent the J for a load-level. To validate the elastic-plastic analysis, we consider the slope of the normalized J-Δ curve from (10) under fully plastic conditions. We now have the slope of the normalized J-Δ curve (under fully plastic conditions), denoted $(Slope)_{th}$ as

$$\frac{d(EJ/Y^2a)}{d(E\Delta/Yl)} = (Slope)_{th} = \frac{2\,l}{\sqrt{3}\,a}. \tag{11}$$

Figure 4 (b) shows the plot of normalized J ($\bar{J}$ for the 3-D meshes) versus normalized Δ. Calculating the slope of the curves from the FE computations from figure 4 (b), we have $(Slope)_{Reg.tet.} = 1.131$, $(Slope)_{Irr.tet.} = 1.120$ and $(Slope)_{Bricks} = 1.134$. We also have for the geometry modeled, $(Slope)_{th} = 1.155$. Thus the slope of $J-\Delta$ curve has a variation of 3% from the theoretical value for the irregular tetrahedral mesh and 2% for the regular tetrahedral mesh.

4.2 Semi-elliptical surface crack in a finite thickness plate

A semi-elliptical surface crack in a finite thickness plate is considered next. Full three-dimensional elastic-plastic analysis of semi-elliptical surface cracks under tensile loading has been performed by Wang [5]. A semi-elliptical crack with a maximum penetration a and a total surface length of $2c$ is in the middle of the plate. The plate has a thickness of t, total width $2b$ and total height $2h$. The dimensional ratios of the crack and plate are given by $a/c = 0.24$, $a/t = 0.6$, $b/t = 8$, and $h/t = 16$. These ratios are the

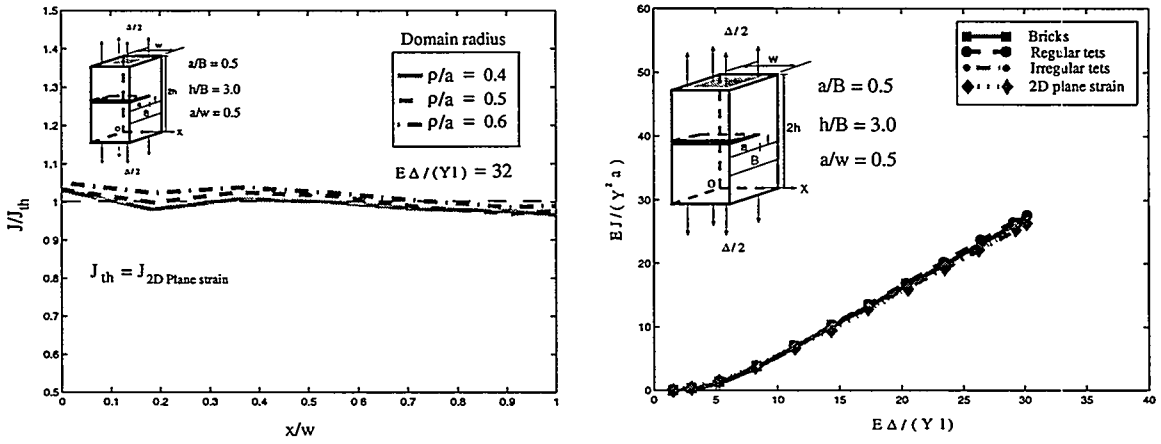

Figure 4: Straight through-thickness crack in plane strain. Elastic/perfectly-plastic material model is used with $Y/E = 0.0011$. (a) Normalized J profile along the crack-front. The values of J are normalized using the J-value obtained from the 2-D plane strain solution for the load level $E\Delta/(Yl) = 32$. The values are shown for three domains of integration: $\rho/a = 0.4$, $\rho/a = 0.5$, and $\rho/a = 0.6$, for the irregular tetrahedral mesh. (b) Variation of normalized J ($\bar{J}$ for the 3-D meshes) with normalized displacement for the FE meshes.

same as the crack geometry analyzed by Wang [5]. The model was loaded by a far-field uniform relative displacement Δ. One-fourth of the specimen geometry is modeled. The Poisson's ratio was set to 0.3 and the Ramberg-Osgood deformation plasticity was used with $\alpha = 1$. Results for a high strain hardening ($n = 5$) case are reported here. Figure 5 (a) shows the variation of J at the symmetry plane normalized by $\sigma_0 \epsilon_0 t$ versus normalized far-field stress, along with the results obtained by Wang [5], for $n = 5$. We can observe from figure 5 (a) that the variation in J at the symmetry plane is less than 3% of the values reported by Wang [5]. Figure 5 (b) shows the J-profile for a stress level $\sigma^\infty/\sigma_0 = 0.975$, normalized by J at the symmetry plane. The J at the free surface is about 20% of the J at the symmetry plane. These profiles are also plotted along with the profiles obtained by Wang [5] and show a close correlation to the reported values.

5 Conclusions

With the development of CAD packages which can create complicated models and mesh them with tetrahedral elements with relative ease, there is a need for a general method to obtain crack-front singularity strengths from tetrahedral element meshes so that the developments in the CAD systems can be directly extended to the whole class of fracture and fatigue crack propagation prediction problems. The practicality of the proposed method lies in its ability to obtain accurate results for elastic-plastic analysis from rather irregular tetrahedral meshes readily obtained from commercially-available CAD packages possessing fairly good meshing capabilities.

A "straightforward" implementation failed to produce acceptably accurate results because of the large gradients within crack-front elements (both those having edge-coincidence with the crack front and those making only vertex contact) introduced by node-based interpolation of domain perturbations of highly localized support. This problem is offset by using perturbations of "extended support," numerical quadrature using analytically-calculated gradients of the perturbation vector field, and interpolation with the use of the nodal support at the boundaries of the model. On the meshes used, the method was shown to be accurate to within $3 - 4\%$ of the theoretical predictions for a wide range of problems.

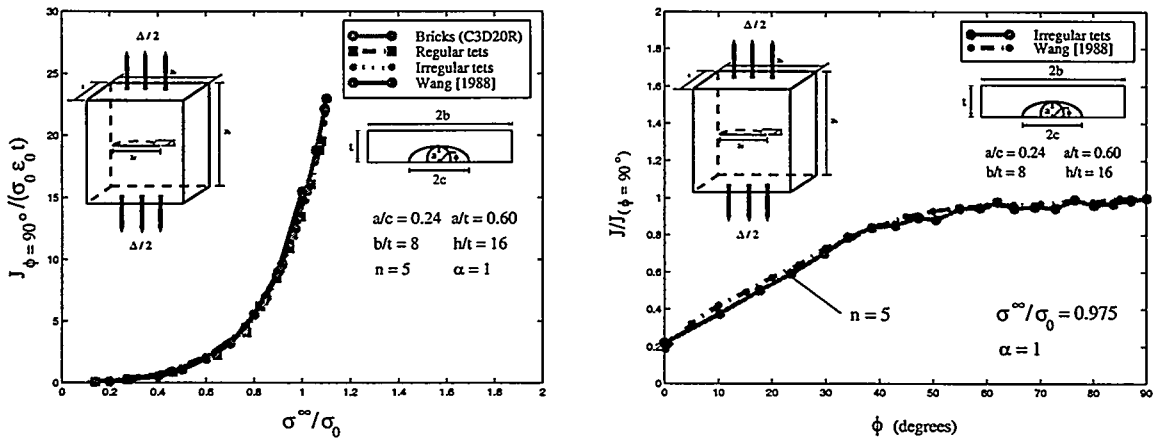

Figure 5: Semi-elliptical surface crack in a finite thickness plate. Ramberg-Osgood deformation plasticity is used with $n = 5$ and $\alpha = 1$. (a) Variation of normalized J at the symmetry plane at different load levels. (b) Variation of J, normalized by J at the symmetry plane, along the crack-front at load level $\sigma^{\infty}/\sigma_0 = 0.975$.

Acknowledgments

This work was supported by the D.O.E under grant number DE-FG02-85ER13331 to MIT. The authors wish to thank Prof. F. A. McClintock for his comments and inputs.

References

[1] Field, D. A., The legacy of automatic mesh generation from solid modeling. *Computer Aided Geometric Design*, 1995, **12**, 651-673.

[2] Rajaram, H., Socrate, S. and Parks, D. M., Application of domain integral methods using tetrahedral elements to the determination of stress intensity factors. Submitted to *Engineering Fracture Mechanics*, 1999.

[3] Raju, I.S. and Newman, J. C., Stress-intensity factors for a wide range of semi-elliptical surface cracks in finite-thickness plates. *Engineering Fracture Mechanics*, 1979, **11**, 817-829.

[4] Rajaram, H., Three-dimensional fracture mechanics computations using tetrahedral finite elements. S. M. Thesis, Massachusetts Institute of Technology, 1999.

[5] Wang, Y., Analysis of fracture initiation in surface-cracked plates. S. M. Thesis, Massachusetts Institute of Technology, 1988.

ON PREDICTING THE TRANSITION IN PROBABILITY OF RARE CLEAVAGE IN DUCTILE CRACKED STRUCTURES

Frank A. McClintock and David M. Parks

Massachusetts Institute of Technology
Cambridge, Massachusetts 02139, U.S.A.

ABSTRACT

If a structure normally undergoes micro-ductile cracking, the probability of cleavage that might shatter the structure should be very small, say < 0.00001. Economic and practical considerations dictate that data be obtained from few, small, quickly tested specimens, perhaps cut from the structure. The results must be extrapolated to the desired very low probability of cleavage in the structure.

Such extrapolation must take into account statistics, size, the compliance of the structure, strain rates, and localized temperature changes. There are theories for the brittle lower shelf and transition regimes, but not for the upper shelf where no macro-cleavage is found in small specimens. An approximate mechanistic model suggests using fractographic examinations for the small fraction of cleaved grains and a micro-mechanical study of the critical agglomeration of cleaved grains that would cause macro-cleavage.

1. INTRODUCTION

1.1 The Problem

There are perhaps a dozen kinds of cleavage transition temperatures. But what is wanted is that of the structure of concern, not of a test specimen. Furthermore, there should be a very low probability ($\approx 10^{-5}$) that the structure will cleave and possibly shatter. Economics dictates that the data be obtained from relatively few, small, quickly tested specimens. The results must be extrapolated, taking into account statistics, size, the compliance of the structure, strain rates, and localized temperature changes. Such theories have been proposed for the brittle lower shelf and transition regimes, but not for the rare cleavage fractures in structures that should be ductile even under design-specified accidents. A method of reaching this objective is outlined here.

1.2 The State of the Art

Typically, the mechanisms of cracking are idealized as a competition between cleavage and the nucleation, growth, and linkage of holes. (But cleavage facets must also link, and hole nucleation may involve cleavage.) A number of analyses could be used. Fracture micro-mechanics at the atomic scale would in principle predict cleavage fracture in structures, but even if the myriad details of initial dislocation and metallurgical structures were known, it would be a hundred years before the crack growth across a 25 mm thick, 200 mm square plate

could be calculated in a day. Fracture micromechanics at the 10-micron scale so far does not deal with observed roughness of 100 to 1000 μm, the inhomogeneous slip in a grain caused by neighboring grains, or the distortions of the yield locus that occur with the non-radial loading around a blunting or growing crack. While micromechanics should be pursued for insight and its future promise, to predict the behavior of large welded structures we also need engineering approximations starting from tests on cm-sized, cracked specimens cut from the weld and from the base metal. These predictions should be based on macromechanics.

Fracture macromechanics characterizes the stress and strain fields in an annular region around a crack tip by a few crack tip driving parameters (DP's). The relations between these and the crack tip response functions (RF's) are found from tests on small specimens. Fracture macromechanics then determines the DP's from the applied loads and deformations, and predicts the resulting crack growth in structures from the RF's. There are three main types of fracture macromechanics, useful with increasing plastic zone sizes relative to the size of the cracked net section. Linear elastic fracture mechanics (LEFM) applies to the initial growth of a pre-existing crack when there is an annular elastic region around the tip of the crack that is large compared to the fracture process zone, to the plastic zone, and to any stable crack growth. Also, the annular region must be small compared to the distance to any other free surface or applied load. Then the stress and strain fields, and hence cracking, are governed by crack tip driving parameters (DP's) consisting of the stress intensity factor K, the mode of loading, and possibly the second-order, constant local tensile stress T parallel to the crack. The initial growth of a macro-crack by cleavage is almost always unstable when LEFM applies. Therefore for Mode I cleavage cracking, the crack tip response function (RF) is simply a critical function: $K_{Ic}(T)$. Non-linear elastic fracture mechanics (NLEFM) applies to the similar situation with power-law, non-linear elasticity giving the Hutchinson, and Rice and Rosengren (HRR) stress and displacement fields. NLEFM can treat crack initiation in elastic-plastic structures (EPFM) if the loading is radial in the sense that the plastic strain increments in an element remain in constant ratios to each other. This requires that any crack growth be small compared to the outer radius of validity of the HRR field. The driving parameters DP are J, the mode, and possibly Shih's triaxiality parameter Q. The local field for quasi-steady growth with linearly hardening fracture mechanics (LHFM) has been found[1], but not the domain of validity nor the connection to the far-field configuration and loading.

Slip line fracture mechanics (SLFM) is a third main type, useful for the desirably ductile structures that require a plastic net section for extended crack growth. SLFM applies when the local fields around a crack tip can be approximated by plane strain, rigid-plastic, nonhardening, slip line plasticity, with only one or two slip lines emanating from the tip. For symmetrical Mode I loading, the DP's are the angle θ_s from the crack direction to the slip lines, the normal stress σ_n across them, and the displacement discontinuity du_s across them for an increment of loading. For the initiation of crack growth the RF of the DP's is u_{si}. The crack tip opening displacement $CTOD_i$ for the initiation of crack growth (see Fig. 1)[2,3] is then

$$CTOD_i = 2u_{si}\cos\theta_s \quad . \tag{1}$$

Similarly, for growth the micro-crack advance per unit slip, dc/du_s, can be converted to the crack tip opening angle $CTOA$:

$$\tan(CTOA/2) = \sin\theta_s / \left(dc/du_s + \cos\theta_s\right) \quad . \tag{2}$$

For a single slip plane typical of mixed mode cracking, the DP's and RF's are similar except that the crack direction is an added RF when expressed relative to the slip line, $\theta_c - \theta_s$ [4].

In process zone computational mechanics (PZCM), there is no annular field between macro-

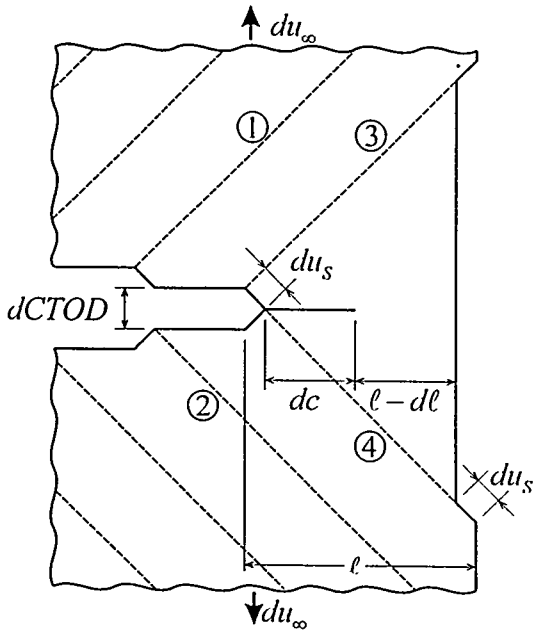

Figure 1. Non-hardening Ligament Reduction by Deformation and Micro-Cracking
Note sliding off and microcracking at crack tip and drawing-in of back face.

mechanics and the fracture process zone. Rather, the process zone is confined to a single plane modeled by a thin layer of finite elements. Fracture is specified by a traction-displacement relation across these elements. If the relation is linear and the deformation is Mode I, the relation can be characterized by a strain-dependent peak stress at the tip of the zone, $\sigma_{mx}(\varepsilon)$, and the crack opening displacement where the traction goes to zero, $CTOD_{mx}$. Linearity may not be sufficiently accurate if cleavage cracking causes an abrupt drop in traction followed by a slow decrease due to tearing of the ligaments between cleavage facets. PZFM has the limitations of not providing closed-form expressions, helpful for interpreting tests on cm-sized specimens. In spite of these difficulties, two-parameter computations have been made by Needleman and by Shih. Further computations should be pursued, general conditions for validity, and the relations to LEFM, NLEFM, and SLFM should be sought. For instance, if there is no plastic flow in the flanks behind the crack tip, Kim[3] has shown there is no effect of the decohering zone on the slip line field, except for a small increase in the limit load.

The effects of finite grain size and statistics in the K- and J-regimes are too numerous to cite here, but some discussion will be given in Sec. 3.5.

2. A SAMPLE PROBLEM

Consider a large plate with a far-field extension u_∞ normal to a surface crack (Fig. 2). Let the crack extend all across the plate so plane strain applies, except near the free surfaces at the ends of the crack. Before initial crack growth, first the K field, then the J field, and possibly an SLFM field applies. For full plasticity and extended growth, SLFM is used as the simplest available field. To illustrate the overall procedure for finding the transition curves of such a structure from small specimen tests, simplify the loadings and responses to one variable each. Thus take both the specimens and the structure to be under pure extension, $u_{\infty sp}$ and $u_{\infty str}$, and take the crack tip DP's to be purely K_I, J, and du_s. That is, ignore bending, triaxiality, (changes in σ_n, and θ_s), even though they do arise from the bending as the decreasing ligament interacts with the plate compliance.

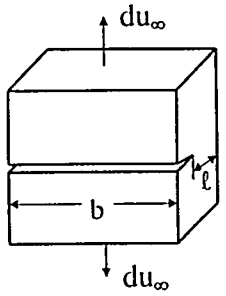

Figure 2. Illustrative Example of a Long Surface Crack in a Plate

3. OPENING AT ORIGINAL CRACK TIP VERSUS APPLIED DISPLACEMENT

3.1 Completely Stable Micro-Ductile Crack Growth in the Specimen

For all the K_I , J , and u_S fields, the increment in opening of the original crack tip, dCT_0OD , can be taken as the crack tip DP. Thus cracking in the specimen can be represented as a single curve of CT_0OD_{sp} versus its far-field half-displacement $(u_\infty)_{sp}$ (see Fig. 3). The curve is found from continuum mechanics or FEM. In the SLFM regime, the shoulders and ends of the specimen are rigid, so the CT_0OD-u_∞ relation is linear with a slope of two. For the initiation of crack growth, the crack tip RF is here simply $CTOD_i$, obtained by 3-D fractography. For growth of the crack in SLFM, the crack tip RF is dc/du_S . It is found by adding to Fig. 3 at $u_{\infty i}$ a second ordinate, namely the crack length as measured by the reduction of the remaining ligament $\ell_i - \ell$. The relation of the ligament reduction to dc/du_S is found by first noting that for this example, with $\theta_S = 45°$ slip, the far field half-displacement du_∞ is given in terms of du_S by

$$du_\infty = du_S / \sqrt{2} \quad . \tag{3}$$

The corresponding ligament reduction is now found from Fig. 1 first in terms of du_S on each 45° slip line by taking into account the drawing-in of the back face and then introducing Eq. 3:

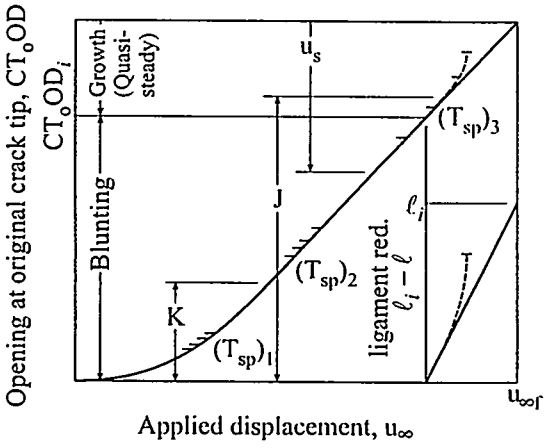

Figure 3. Opening at Original Crack Tip, CT_0OD , versus Far-field Displacement, u_∞
For initial and continuing micro-ductile crack growth, with
regimes for valid K-, J-, and u_S- fracture mechanics, as well as cleavage and instability cut-offs.

$$-d\ell = 2\frac{du_s}{\sqrt{2}} + \frac{dc}{du_s}du_s = 2du_\infty + \frac{dc}{du_s}\sqrt{2}du_\infty \;\; ; \; -\frac{d\ell}{du_\infty} = 2 + \sqrt{2}\frac{dc}{du_s} \quad . \tag{4}$$

Scatter in $CTOD_i$ and in dc/du_s during micro-ductile fracture are ignored in this example. If there is no prior instability or cleavage, the specimen fails when the ligament becomes zero.

The curves in Fig. 3 of CTOD and then $\ell_i - \ell$ versus u_∞ depend on the specimen size through the remaining ligament at initiation, ℓ_i , and through the far-field compliance. They also depend on the temperature and loading rate, especially if changed from quasi-static to rapid ("impact") rates. Here, all specimens will be regarded as rapid-loaded, so rate effects will be ignored until considering the transition behavior of a nearly static structure.

In summary, up to initiation $CTOD(u_\infty)$ is found from analysis or the FEM. $CTOD_i$ is found from 3-D fractography. It appears that the variables $\ell_i - \ell$ and CT_0OD must be found ultrasonically or by sectioning at various stages. Curves such as Fig. 3, up to instability, cleavage, or final penetration, must be found for each temperature in the transition regime.

3.2 Instability

If the load drop per unit extension across the net section decreases, for instance due to damage ahead of the crack giving a smaller crack opening angle, or if the stiffness of the loading decreases at low loads, instability may intervene before crack penetration through the thickness. The resulting upward curvature of the plot of CT_0OD versus u_∞ is shown by a dashed line in Fig. 3. When the applied extension per unit load drop goes to zero, the system becomes unstable even if the surroundings are infinitely stiff and the load is still finite.

3.3 Cleavage Cracking, with Variability

Representative experimental variability in cleavage is shown by the horizontal marks on the curve of Fig. 3, grouped by the various nominal specimen temperatures T_{sp} . Cleavage may occur when the crack tip is K-, J-, or u_s-controlled, depending on temperature. Also, it may occur before or during micro-ductile crack growth, or not at all, as the structural engineer hopes.

3.4 Deriving the Material-determined Reference Probability Plot from the Specimen Tests

This requires correcting the data of Fig. 3 for local temperature and statistical effects: a) In pre-cracked impact tests on a tough structural steel (ε = 0.25, σ = 600 MPa), the crack tip temperatures T_{tip} may be 15-40°C higher than the pre-test specimen temperature T_{sp} . For initiation, $T_{tip} - T_{sp}$ depends strongly on the size of the plastic zone and on blunting. (Note that blunting effects may be minimized in low-cycle fatigue, which occurs in earthquakes or repeated service loads, with the crack approaching its critical length.) For growing cracks, $T_{tip} - T_{sp}$ depends on the crack velocity and the strength and sharpness of the accompanying shear bands. b) The probability of cleavage is affected by the length of the crack front in plane strain, $b_{pl\ stn}$. This varies from specimen to specimen because $b_{pl\ stn}$ varies with the CTOD through the end effects caused by the shear lip, for example. The data of Fig. 3 must be corrected to a common reference length b_{ref} . For small corrections,

$$CTOD_{i\,ref} = CTOD_{i\,sp} + \left(\frac{\partial CTOD}{\partial T}\right)_P \left(T_{ref} - T_{tip}\right) + \left(\frac{\partial CTOD}{\partial P}\right)_T \left(\frac{\partial P}{\partial b}\right)_T \left(b_{ref} - b_{pl\,stn}\right) \quad . \tag{5}$$

For an initial iteration, the first two partial derivatives can be obtained from Fig. 3. The statistical size effect , $(\partial P/\partial b)_T$, comes from the theory for the assumed distribution function.

The probability P_n for the n^{th} specimen can be estimated from order statistics:

$$P_n = n / (n_{max} + 1) \quad . \tag{6}$$

Equations 5 and 6 give the physical initiation probabilities $P(T_{ref}, CTOD_{i\ ref}, b_{ref})$ from the specimen data $P(T_{sp}, CTOD_{i\ sp}, b_{pl\ stn})$ such as Fig. 3.

The probabilities of cleavage before and during crack growth under the reference conditions are plotted in Fig. 4 as CT_oOD versus T_{ref} for lines of constant P from Eq. 6. For simplicity, the displacements $CTOD_i$ and CT_oOD_f are assumed independent of temperature. The original data and its corrections to T_{ref} and b_{ref} are shown as dots connected by lines.

As micro-ductile crack growth begins, the tip temperatures decrease, and the temperature corrections beome less. It is assumed here that the increase in probability of cleavage with CT_oOD also becomes less, so the lines of constant probability bend sharply upward. The final corrected points are connected by dashed lines where data are limited. Note that data should be taken at closely spaced temperatures near initiation and in the crack growth region (near the upper shelf fracture appearance transition).

Crack penetration depends on the thickness. The probabilities of fracture converge to a single line, since scatter in micro-ductile cracking has been neglected.

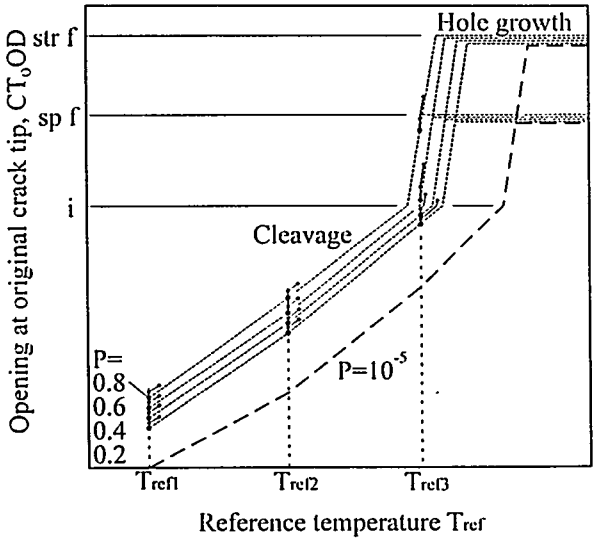

Figure 4. CT_oOD versus Temperature Corrected to Reference Conditions
Lines of constant probability of cleavage.
Bends occur at initial micro-ductile crack growth, taken independent of temperature.

3.5 Extrapolating the Reference Plot to the Required Cleavage Probability before Initiation

Models for estimating $CTOD_c(P)$ are too numerous to cite here. In spite of the fact that the triggering of cleavage fracture is often a cooperative rather than a single event, extreme value (EV) statistics are usually assumed. Note that EV distributions are not necessarily approached by the extremes of large samples (as the normal distribution is approached by the means of large samples). Further, a change of variables shows that in LEFM if the distribution of crack lengths

is EV, the distribution of strengths is not. Rather, EV distributions are ones whose underlying form remains unchanged with sample size. They involve three parameters. In principle, for either of the lower two reference temperatures of Fig. 4, these parameters could be estimated from the distribution of CTOD's of the specimens, and then the extrapolation made to the desired probability. In practice, the spread of such estimates is hopeless. Weibull has said that to distinguish a log-normal distribution from the most closely matching EV distribution would require a sample size of 20,000! So one must make a number of different assumptions based on experience, and then again from experience, select a number based on those results.

At temperatures T_{ref3} and above, extrapolation fails because the critical initiation data are truncated or non-existent. Again in principle, one might try to estimate the temperature-dependence for each of the EV parameters at lower T_{ref}'s and use those to get $CTOD_i(P)$. For growth, the means of estimation will be discussed in Sec. 4.2 in connection with structures.

4. FINDING THE ALLOWABLE $CT_0OD(P)$ FOR A STRUCTURE

4.1 The Cleavage Probability before the Initiation of Crack Growth

For initiation, the reference temperature for the structure could be found from the structural conditions as for the specimens, but also taking into account the effects of deformation rate, perhaps by the rate modified temperature. With a range of reference probabilities before initiation plotted in Fig. 4, the appropriate CTOD before initiation could be read. Mechanics could then give the allowable crack length in the structure for its geometry and loading. An iteration might be needed to account for the volume ahead of the crack, using EV ideas. But this all deals with relatively brittle structures, which cleave before the initiation of micro-ductile crack growth. We finally turn to the upper right corner of Fig. 4, where all specimens have been totally macro-ductile, but some structures will cleave during macro-ductile crack growth.

4.2 The Required Cleavage Probability during Crack Growth

An approximate model of the statistics of cleavage during plastic crack growth was based on a probability of cleavage of an individual grain, p_g, and the assumption that unstable macro-cleavage cracking occurs when a small patch of area A_p of neighboring grains have cleaved[5]. The number of independent patches per unit area was taken to be A/A_g to $(A/A_g)/(A_p/A_g)$. For a through-crack in a pressure vessel, the surface area might be $A = 20\text{x}200 \text{ mm} = 4\ 10^3 \text{ mm}^2$. For a 20 μm grain size, with $A_g = 4\times10^{-4} \text{ mm}^2$, this would give $A/A_g = 10^7$. The allowable probability of a macro-cleavage fracture might be, say, $1 - P_{srv} = 10^{-6}$. Since the grains per patch that would trigger macro cleavage appear to be $A_p/A_g = 1$ to 10, the approximation[5]

$$\frac{A}{A_g} = \left(1 \text{ to } \frac{A_p}{A_g}\right)\frac{1-P_{srv}}{p_g^{A_p/A_g}} \quad ; \quad p_g = \left[\left(1 \text{ to } \frac{A_p}{A_g}\right)\frac{1-P_{srv}}{A/A_g}\right]^{1/\left(A_p/A_g\right)} \quad . \tag{7}$$

shows that the material-, stress-, and temperature-dependent grain cleavage probability would be $p_g = 10^{-13}$ to 0.06. Clearly, the critical number of grains per patch, A_p/A_g, is essential. Further studies to clarify the analysis should include the following:

a) From stably tearing plates, measure the fraction of grains cleaved, p_g.

b) From fractography and from micromechanics, including dynamics and rate effects, estimate the patch size (area of contiguous cracked grains) needed to trigger macroscopic cleavage for the conditions of the stably growing plastic crack.

c) In Eq. 7, use those numbers, along with the desired P_{srv}, to estimate the allowable area swept out before macroscopic, unstable cleavage.

For example, if one can determine from fractography that at a given temperature the probability of cleavage of an individual grain is no more than $p_g = 10^{-3}$, if a patch size of $A_p/A_g = 4$ is required for macro-cleavage, and if the probability of survival is to be at least 0.999999, Eq. 7 indicates that a plastic crack must not grow beyond $A/A_g = (1 \text{ to } 4)\times 10^6$. This means that for a grain size of 20 μm, the area swept out by the plastic crack must be limited to $A < 400$ to 1600 mm^2, a rather severe restriction for steel structures.

The difficulty of determining the critical patch size, Step (b), seems to mean that further studies are essential for a method to design of ductile structures of high reliability.

CONCLUSION

The crucial step in assuring very low probabilities of cleavage in normally ductile structures is predicting the probability of rare macro-cleavage during micro-ductile crack growth. An approximate analysis provides a method of making such estimates when the macro-cleavage is due to a critical patch of A_p/A_g cleaved grains.

ACKNOWLEDGEMENTS

The support of the Office of Basic Energy Sciences of the DOE and of Lockeed Idaho Technologies is deeply appreciated. Warm thanks are also given to a number of colleagues and graduate students: W. Reuter, N. Ishikawa, O. Muragishi, H. Rajaram, and K. Bass.

CITED REFERENCES

1. P. PONTE CASTAÑEDA,, "Asymptotic Fields in Steady Crack Growth with Linear Strain-Hardening", *J. Mech. Phys. Solids* 35, 227-268 (1987).

2. F. A. McCLINTOCK, Y.-J. KIM, and D. M. PARKS, "Tests and Analyses for Fully Plastic Fracture Mechanics of Plane Strain Mode I Crack Growth", *Fracture Mechanics: 26th Volume*, W. G. Reuter, J. H. Underwood, and J. C. Newman, eds., ASTM STP 1256, Am. Soc. Test. Mater., Philadelphia, 199-222 (1995).

3. F. A. McCLINTOCK, Y.-J. KIM, and D. M. PARKS, "A Criterion for Plane Strain, Fully Plastic, Quasi-Steady Crack Growth", *Int. J. Fracture* 72, 197-221 (1995). .

4. F. A. McCLINTOCK, K. L. KENNEY, S. JUNG, W. G. REUTER, and D. M. PARKS, "Asymmmetric, Fully Plastic Crack Growth Mechanics and Tests for Structures and Piping", *Proceedings of Symposium on Development, Validation, and Application of Inelastic Methods for Stuctural Analysis and Design*, R. F. Sammataro and D. J. Ammerman, eds, PVP - 343, Am. Soc. Mech. Eng., New York, 153-167 (1996).

5. F. A. McCLINTOCK, "A Three-dimensional Model for Polycrystalline Cleavage and Problems in Cleavage after Extended Plastic Flow or Cracking", *Cleavage Fracture: George R. Irwin Symposium*, K. S. Chan, ed., TMS, Warrendale PA, 81-94 (1997).